Experimental determination of latent hardening coefficients in FeMnNiCoCr

Y. Wu[a], M. Bönisch[a], S. Alkan[a], W. Abuzaid[b], H. Sehitoglu[a],*

[a] Department of Mechanical Science and Engineering, University of Illinois at Urbana-Champaign, 1206 W. Green St., Urbana, IL 61801, USA
[b] Department of Mechanical Engineering, American University of Sharjah, PO Box 26666, Sharjah, United Arab Emirates

ABSTRACT

The equi-atomic FeMnNiCoCr high entropy alloy is attracting unprecedented attention due to its exceptional strain hardening behavior extending to large strains and to low temperatures (77K). In this paper, we analyze the nano- to macroscale deformation response of FeMnNiCoCr single crystals and explain variations in strain hardening based on the activation of different twin and slip systems and their interactions. We experimentally determine the latent and the self hardening moduli upon twin-twin, slip-twin, twin-slip and slip-slip interactions. Choosing single crystal orientations that isolate these interactions enables the evaluation of the pertaining hardening moduli without ambiguity. Differing from the earlier experimental approaches employed, which necessitate sample reorientation to quantify the self and latent hardening coefficients, in this work, we demonstrate a novel framework where plastic straining is implemented in a monotonic fashion entailing the latent and primary systems to operate simultaneously. To extract the hardening moduli and to characterize the twin-twin, slip-twin, twin-slip and slip-slip interactions on experimental grounds, $<111>_{\text{tension}}$ and $<001>_{\text{compression}}$ single crystalline samples are studied by high resolution digital image correlation, electron backscatter diffraction and transmission electron microscopy techniques. The results demonstrate that the magnitude of residual Burgers vectors play a key role in explaining the experimental hardening trends.

1. Introduction

1.1. Background and motivation

The equi-atomic FeMnNiCoCr high entropy alloy (HEA), originally discovered by Cantor et al. (2004), has become the most widely studied composition in this class of alloys. It forms a face-centered cubic (fcc) solid solution and is close enough to an ideal solution that the configurational part of the mixing entropy prevents formation of secondary solid solutions and intermetallics during preparation from the melt (Otto et al., 2013b). Its key mechanical attributes are superior tensile strength (~1 GPa (Gali and George, 2013; Otto et al., 2013a; Wu et al., 2015)), exceptional ductility (60–70% (Otto et al., 2013a; Wu et al., 2015)) and fracture toughness (exceeding 200 MPa$\sqrt{\text{m}}$ (Gludovatz et al., 2014)) at cryogenic temperatures (77K). These desirable properties have been typically associated with the activation of deformation twinning (Abuzaid and Sehitoglu, 2017; Zhang et al., 2015), particularly at low temperatures. Furthermore, the deformation twins are observed to promote strain hardening substantially. Earlier literature (Laplanche et al., 2016; Otto et al., 2013a) demonstrates that the polycrystalline microstructure exhibits extraordinarily high strain

---

hardening coefficients at large strain levels (∼3 GPa above 15% strain). However, the origins for such high strain hardening is still yet to be established. To that end, this work interrogates the strain hardening mechanisms in equi-atomic FeMnNiCoCr HEA.

Throughout this work, following points will be scrutinized to build a comprehensive understanding on the strain-hardening behavior of FeNiCoCrMn HEA: (i) dislocation reactions accompanying twin-twin interactions produce sessile residual Burgers vectors which act as barriers against dislocation glide; and (ii) twin-twin interactions can enhance the level of hardening and result in large hardening coefficients at high strains closely linked with the number of active systems. To accomplish this task, we conduct uniaxial tension and compression experiments employing digital image correlation (DIC) on a set of single crystal orientations which are conducive to twinning. This approach allowed us to quantify the latent hardening moduli due to the interactions between primary and latent twin systems. Overall, this work provides a deeper insight into the strain hardening mechanisms of FeMnNiCoCr HEAs at low temperatures.

In polycrystalline materials, the distribution of crystal orientation, matrix constraints and variety of reactions taking place at grain boundaries (i.e., formation of dislocation pile-ups (Laplanche et al., 2016; Otto et al., 2013a) and cross-boundary twins (Hazeli et al., 2013) at grain boundaries) can complicate the analysis and hinder the ability to unambiguously pinpoint the mechanisms prevailing on the hardening response. These reasons have led us to utilize single crystalline samples throughout this work to quantify the critical stress levels for the initiation of slip, nucleation of twinning, as well as the levels of their interaction on the corresponding strain hardening behavior. This allowed us to characterize the constitutive response of the FeMnNiCoCr HEA by eliminating the grain boundary constraint effects.

On the other hand, the strain hardening response of single crystalline FeNiCoCrMn is also of complicated nature inasmuch multiple deformation mechanisms (i.e., slip, twinning, or both (Patriarca et al., 2013)), may participate with the proceeding plastic deformation. It is evident that the contribution of these mechanisms, which is typically reflected as slope changes in the stress strain curve, alter the individual flow stress levels on each slip and twin system. This can be broken down to self hardening of the active system(s) in addition to latent hardening, which is referred to as the increase of the resistance to plastic deformation on latent systems upon deformation on the primary system (Franciosi, 1985; Wu et al., 1991). The rate-independent crystal plasticity of Mandel (1965) and Hill (1966) is adopted in this work to determine the corresponding hardening moduli. To that end, a linear hardening rule in which the shear stress increment on the α-system, $d\tau^{(\alpha)}$, is related to the shear strain increment on the β-system, $d\gamma^{(\beta)}$ by a hardening matrix $h_{\alpha\beta}$, i.e. $d\tau^{(\alpha)} = \sum_{\beta=1}^{N} h_{\alpha\beta}d\gamma^{(\beta)}$, is employed. Though the hardening matrix, including both self hardening (diagonal terms) and latent hardening (off-diagonal terms) moduli, is of paramount importance for a predictive crystal plasticity modeling (Bertin et al., 2014; Iadicola et al., 2012; Kireeva et al., 2016; Pham et al., 2017; Tadano et al., 2016), an accurate characterization technique for it is yet to be established in the literature. This paper presents a novel approach to accomplish this task by pinpointing the local strain evolution on the active twin and slip systems via DIC as a function of applied stress.

1.2. Constitutive equations for latent hardening

A crystal plasticity framework that incorporates pure as well as mixed interaction contributions of slip and deformation twinning to the strain hardening in FeNiCoCrMn HEA can be expressed as follows:

$$d\tau^{(\alpha')}_{critical} = (1 - \sum_{k}^{N} f^{(k)}_{twin}) \sum_{\beta'}^{N} h^{slip-slip}_{\alpha'\beta'} d\gamma^{(\beta')}_{slip} + \sum_{\beta}^{N} h^{slip-twin}_{\alpha'\beta} df^{(\beta)}_{twin} \gamma^{fcc}_{twin}$$

$$\underbrace{\qquad\qquad}_{\text{slip-slip}} \qquad \underbrace{\qquad\qquad}_{\text{slip-twin}} \tag{1a}$$

$$d\tau^{(\alpha)}_{critical} = (1 - \sum_{k}^{N} f^{(k)}_{twin}) \sum_{\beta'}^{N} h^{twin-slip}_{\alpha\beta'} d\gamma^{(\beta')}_{slip} + \sum_{\beta}^{N} h^{twin-twin}_{\alpha\beta} df^{(\beta)}_{twin} \gamma^{fcc}_{twin}$$

$$\underbrace{\qquad\qquad}_{\text{twin-slip}} \qquad \underbrace{\qquad\qquad}_{\text{twin-twin}} \tag{1b}$$

where α' and β' denote the slip systems, α and β designate the twinning systems, $d\gamma^{(\beta')}_{slip}$ is the slip shear strain increment of system β', $f^{(k)}_{twin}$ is the volume fraction of twinning system k, $df^{(\beta)}_{twin}$ is the change of twin volume fraction of system β, and γ^{fcc}_{twin} denotes the intrinsic twinning shear (0.707 for {111}<112> twins in an fcc lattice). In Equations (1a) and (1b), $h^{slip-slip}_{\alpha'\beta'}$, $h^{slip-twin}_{\alpha'\beta}$, $h^{twin-slip}_{\alpha\beta'}$ and $h^{twin-twin}_{\alpha\beta}$ represent the hardening moduli associated with slip-slip, slip-twin, twin-slip and twin-twin interactions. In the most general case for an fcc lattice that deforms on 12 {111}<110> slip systems and by 12 {111}<112> twin modes the four hardening matrices $\{h^{slip-slip}_{\alpha'\beta'}\}$, $\{h^{slip-twin}_{\alpha'\beta}\}$, $\{h^{twin-slip}_{\alpha\beta'}\}$ and $\{h^{twin-twin}_{\alpha\beta}\}$ contain in total 576 hardening moduli $h_{\alpha\beta}$. Their experimental determination is a formidable task and has been elusive given their sheer number.

It is feasible to isolate each of the contributing terms in Equation (1) and calculate the corresponding strain hardening coefficients using single crystals where the certain slip or twin systems can be activated by varying the crystallographic orientation and the loading sense (tension vs. compression). For instance, when only twin-twin interactions are considered (such as those observed for compression along <001> and tension along <111>, as presented in Section 3), Equation (1) can be simplified as follows:

$$d\tau^{(\alpha)}_{critical} = \sum_{\beta=1}^{N} h^{twin-twin}_{\alpha\beta} df^{(\beta)}_{twin} \gamma^{fcc}_{twin} \tag{2}$$

Although there are 12 {111}<112> potential twin systems in an fcc crystal, considering their Schmid factors, only a few of these systems become activated under uniaxial loading. For example, Schmid factor analysis predicts only 4 and 3 systems to be activated for <001>_compression (max. Schmid factor $m = 0.47$) and <111>_tension ($m = 0.31$) samples respectively (Karaman et al., 2001). On

the other hand, it is to be emphasized that while the latent hardening can be interpreted (comparably) readily when two systems are present it becomes increasingly complex as the number of active systems grows. The methodology followed to accomplish this task will be addressed in Section 3 in detail.

1.3. Current approach vs. previous studies

On experimental grounds, numerous works have been reported in the literature on slip induced latent hardening in cubic metals including copper, aluminum, iron and silver via employing single crystals (Franciosi, 1983, 1985; Franciosi et al., 1980; Jackson and Basinski, 1967; Kocks, 1970; Kocks and Brown, 1966; Nakada and Keh, 1966; Wu et al., 1991). In these experimental studies, latent hardening experiments were performed such that primary and latent slip were nucleated separately in two consecutive experiments. The amount of latent hardening during the primary test was indirectly measured from the ratio between the critical stress extrapolated from the secondary test and the maximum stress at the end of the primary test. The corresponding modification of Schmid factors introduces an artificial loading history effect which is absent under monotonic loading conditions. Consequently, this earlier methodology allows for only an indirect quantification of latent hardening. Within the framework of this method, Kocks (1970) predicted a range of 1.0–1.4 for the ratio between the latent and self hardening moduli, which is frequently employed as a constitutive parameter in crystal plasticity modeling. On the other hand, it is important to note that this measurement procedure suppresses the primary slip throughout the secondary loading step as the change of crystallographical loading axis lowers the corresponding Schmid factor. Consequently, this indirect measurement technique for latent hardening by inducing single slip on distinct systems throughout the two loading steps represents a rather idealized scenario. As a remedy, in the present work, we employ a novel experimental framework wherein the plastic deformation proceeds under monotonic loading conditions allowing for the interaction of multiple active systems with further straining. We believe that this proposed experimental procedure overcomes the ambiguity in the strain hardening levels associated with the sample re-orientation operation implemented in two-step experiments. As an immediate consequence of the monotonic plastic strain accommodation in this novel method, both the self and latent hardening moduli can be determined for the loading configurations in which multiple systems interact. To that end, the effective hardening slope of corresponding segments of the experimental stress-strain curves can be directly employed to extract both the latent and self hardening moduli.

Though deformation twins are expected to play a significant role in the effective strain hardening slope of low stacking fault energy fcc materials within the framework of slip-twin, twin-slip, twin-twin interactions, a comprehensive study is yet to be carried out except for a limited number of polycrystalline materials (Cherkaoui, 2003; Salem et al., 2005). The efforts for determining hardening moduli from the stress-strain curves of these corresponding polycrystalline samples can only reflect the effective hardening properties with a limited distinction between the hardening moduli of individually interacting coplanar and non-coplanar systems. To that end, the hardening moduli (self and latent) for specific pairs of interacting systems could not be determined through these models, which is of significant importance in characterizing the contribution of potential deformation modes on mechanical grounds.

The present work establishes a framework to quantify for the latent and self hardening moduli for twin-twin, slip-twin, twin-slip and slip-slip interactions in a systematic fashion based on synchronized measurement of resolved stresses and the corresponding local strain fields along the interacting twin and slip systems in single crystalline FeMnNiCoCr samples. This novel approach enables us to clarify the individual role of interacting systems (either twin or slip) without any prior assumption or empiricism. The previous study by Abuzaid and Sehitoglu (2017) on the fcc FeMnNiCoCr HEA made clear that the plastic deformation was accommodated by double slip on $(111)[\bar{1}01]$ and $(\bar{1}11)[\bar{1}0\bar{1}]$ systems for $<149>_{tension}$ loading. On the other hand, in the $<122>_{tension}$ case, the nucleation of a single slip system, $(\bar{1}11)[01\bar{1}]$, was revealed at the early stage of deformation and then followed by the activation of a twin system, $(1\bar{1}1)[\bar{2}\bar{1}1]$, at a higher strain level. In this study, we focus on the hardening response of $<111>_{tension}$ and $<001>_{compression}$ samples as both of these samples are conducive to twinning as confirmed by our experiments. Based on the experimental stress-strain data from the present and our earlier work (Abuzaid and Sehitoglu, 2017), the specific $h_{\alpha'\beta'}^{slip-slip}$, $h_{\alpha'\beta}^{slip-twin}$, $h_{\alpha\beta'}^{twin-slip}$ and $h_{\alpha\beta}^{twin-twin}$ values are evaluated for the pairs of interacting systems in the $<149>_{tension}$, $<122>_{tension}$, $<111>_{tension}$ and $<001>_{compression}$ samples, respectively. These quantitative analyses demonstrate that the contribution of slip and twinning on the effective hardening moduli, i.e. $d\sigma/d\varepsilon$, is substantially different. In particular, we note that the effective hardening slope in the case of interaction between slip and twinning derived from the $<122>_{tension}$ case, ~ 0.5 GPa, is far greater than that of slip-slip interaction derived from the $<149>_{tension}$ case, ~ 0.01 GPa. In this study, we demonstrate the corresponding effective hardening slope due to twin-twin interactions is on the order of 2–3 GPa, which is much higher than those of slip-twin (twin-slip) and slip-slip cases. Similar results have been demonstrated by Patriarca et al. (2013) who investigated the strain hardening response of body-centered cubic (bcc) FeCr single crystals and showed that twin-twin interactions impart considerably higher hardening, ~ 9 GPa, than slip-slip, ~ 0.05 GPa, and slip-twin/twin-slip, ~ 1 GPa, interactions. These results suggest that the contribution of twin-twin interactions to the overall material strengthening is the most significant among the interaction mechanisms considered. To that end, we focus on twin-twin interactions and the associated hardening in this work. Furthermore, a detailed quantitative analysis of hardening due to slip-slip, slip-twin and twin-slip interactions are also provided in the Appendix A and B.

1.4. Considerations of the residual Burgers vector

As aforementioned, the interactions between slip and twinning can impart various strengthening levels to the material. Such diverse strain hardening behaviors at macroscale can be better rationalized by the corresponding dislocation reactions at nanoscale. The interactions between slip and twin systems have been investigated in-depth in many previous undertakings (Ezaz et al., 2010; Jin

et al., 2008; Mahajan and Chin, 1973, 1974; Remy, 1977, 1981; Sangid et al., 2012). The noteworthy outcome of slip-twin and twin-twin interactions is that the impinging dislocation leaves a residual Burgers vector, $\underline{b}^r$, on the obstacle twin interface after the dislocation reaction. This residual dislocation, similar to a Lomer-Cottrell lock, is sessile and forms a barrier to the dislocation glide on the twin plane, which imparts strengthening to the material (Friedel, 1955; Mott, 1952; Seeger et al., 1957). The magnitude of such a residual dislocation, $|\underline{b}^r|$, is expected to have an important implication on the strain hardening behavior of the material. According to other studies (Chowdhury et al., 2016; Ezaz et al., 2010; Sangid et al., 2012), $|\underline{b}^r|$ of slip-twin interactions for an fcc alloy where an incident Shockley partial incorporates into the barrier twinning boundary usually varies from $0.24a$ to $0.53a$ (a is the lattice constant). In this study, we show that the $|\underline{b}^r|$ generated from twin-twin interactions can reach an order of $1.22a$, which is undoubtedly higher than those of slip-twin interactions. This result is also consistent with the higher strain hardening level associated with twin-twin compared to slip-twin and twin-slip interactions. Overall, all these experimental investigations imply the key role of dislocation-interactions in contributing to high strain hardening. In the present analysis, we demonstrate that residual Burgers vectors, which result from different twin-twin interactions and thus exhibit varying magnitudes, impart different strengthening levels, i.e. hardening moduli $h_{\alpha\beta}$ ($\alpha \neq \beta$).

In summary, we conducted uniaxial tensile and compressive experiments on FeMnNiCoCr single crystals at liquid nitrogen temperature (77K) in this work. Initial tests (presented in Appendix A and B) were performed on <149> and <122> crystals in tension to selectively activate double slip at the onset of plastic yielding and single slip followed by twinning, respectively. These tests revealed higher latent hardening moduli for slip-twin/twin-slip interactions than for slip-slip interactions. Based on these first results, we selected single crystals whose loading axes are close to <111> and <001>. It has been well-established that these orientations are favorable for twinning in tension and compression, respectively, in fcc materials (Karaman et al., 2001). The main body of this article presents and analyzes their twinning-induced hardening behavior and pays close attention to residual Burgers vectors associated with the twin interactions observed. For this purpose, ex-situ high resolution digital image correlation (DIC), electron backscatter diffraction (EBSD) and transmission electron microscopy (TEM) were performed on the deformed specimen to identify the deformation mechanisms and reveal twin-twin interactions at the nanoscale. Finally, we calculate the hardening moduli $h_{\alpha\beta}$ based on the experimental results of <001> and <111> loading cases where dominant twinning activities are confirmed. In parallel, we evaluate the magnitude of the residual Burgers vectors formed by the observed twin-twin interactions. The corresponding $|\underline{b}^r|$ varies with different twin-twin interactions and is indicative of the associated hardening. We also show that the hardening moduli associated with slip-twin, twin-slip and slip-slip interactions (Abuzaid and Sehitoglu, 2017) are much smaller than those associated with twin-twin interactions for fcc FeMnNiCoCr HEA.

2. Materials and experimental methods

Single crystals of the equiatomic FeMnNiCoCr alloys were grown using the Bridgman technique in an inert gas atmosphere. The alloys were homogenized at 1473K for 24 h and solutionized at 1373K for 1 h followed by oil quenching. To induce twin-twin interactions, we consider single crystals with the loading axis along the $[11\bar{1}]$ and $[100]$ crystallographic directions (hereafter referred to as $[11\bar{1}]_T$ and $[100]_C$). These orientations have been confirmed by the Euler angles procured via EBSD.

Both uniaxial tensile and compressive experiments were performed at 77K with the specimen, grips, and extensometer submerged in a liquid nitrogen bath. Samples were deformed in strain control during loading and load control during unloading. An extensometer was used to measure the strain evolution and each sample was loaded incrementally up to a total strain of $\sim 20\%$. High resolution ex-situ DIC was performed on deformed specimens at the end of each load increment, since in-situ DIC images are inaccessible when the specimen is submerged in the liquid nitrogen bath. It is important to note that additional polishing is required at the end of each load increment in order to re-establish a satisfying speckle pattern for further measurement. Therefore, the DIC strain contour shown in this study represents the strain increment between loading cycles. The total strain accumulation was tracked using an extensometer in this study. Both reference and deformed images were taken with an optical microscope with $10\times$ magnification which corresponds to a spatial resolution of 0.44 μm/pixel. To cover the entire width of the specimen, 5 images were captured with approximately 30% overlap. 3 rows of images were captured to enlarge the area of interest ($\sim 3\,mm \times 1\,mm$). Then, DIC was performed on each pair of images (reference and deformed) with a subset size of 35×35 pixels and later the results were stitched together following the procedure detailed in the previous study by Carroll et al. (2010).

Transmission electron microscopy (TEM) specimens oriented perpendicular to the loading direction were lifted out from the deformed samples and thinned by focused ion beam in a FEI Helios 600i DualBeam. A JEOL 2010 LaB$_6$ TEM optimized for diffraction and high sample tilts was used to identify active slip and twin planes and to image deformed microstructures. A 3-dimensional model of an interaction site of two twins was created from a tilt series using the UCSF Chimera package (Pettersen et al., 2004). To this end, projections of the interaction site were recorded over a tilt range of 50° in two-beam conditions and the model compared with the projections.

For ease of discussion, the designations of the 12 possible twin systems for an fcc crystal and the corresponding Schmid factors for the orientations studied are tabulated in Table 1. The Schmid factors are calculated based on the original crystal orientation from EBSD measurement. According to the Euler angles, the crystallographic loading directions of the specimens are [0.5791 0.4640–0.6703] and [0.9998–0.0204 -0.0012], which are denoted as $[11\bar{1}]_T$ and $[100]_C$, respectively, in this paper. Those twinning systems potentially active based on the Schmid law are highlighted for each case. We would like to point out that the Taylor-Schmid law, often referred to as the Schmid law, is based on the early works of Taylor (Taylor et al., 1923) and Schmid (Schmid and Boas, 1935). In this study, we observed three active twin systems in the $[100]_C$ case and two systems in the $[11\bar{1}]_T$ case based on experimental measurements.

Table 1
Designations of all 12 twin systems in an fcc crystal subject to tension and compression along the nominal $[11\bar{1}]_T$ and $[100]_C$ loading orientation. The Schmid factors correspond to the exact loading orientation determined from the Euler angles. Twin systems with high Schmid factors are highlighted for each case.

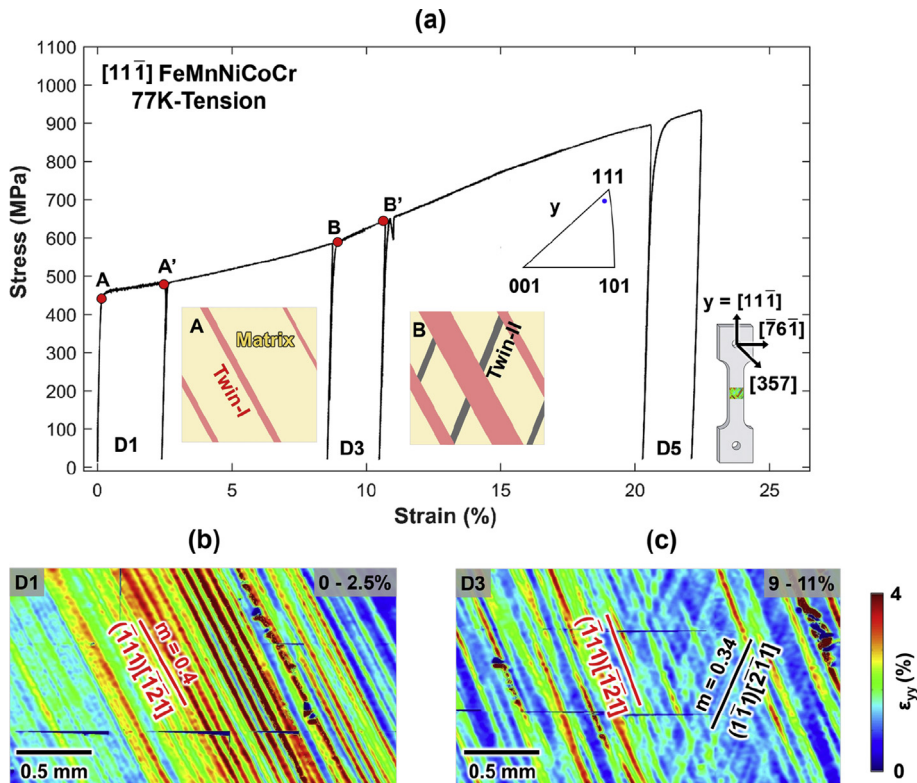| No.	Twin system	Nominal loading direction	
		$[11\bar{1}]_T$	$[100]_C$
		Schmid factor	Schmid factor
1	$(\bar{1}\bar{1}1)[\bar{1}\bar{1}\bar{2}]$	−0.12	−0.23
2	$(1\bar{1}1)[1\bar{1}\bar{2}]$	−0.19	−0.25
3	$(\bar{1}11)[\bar{1}1\bar{2}]$	−0.23	−0.25
4	$(1\bar{1}1)[121]$	−0.11	−0.23
5	$(\bar{1}\bar{1}1)[\bar{1}21]$	0.13	−0.24
6	$(111)[1\bar{2}1]$	−0.09	−0.24
7	$(\bar{1}11)[\bar{1}\bar{2}1]$	**0.4**	−0.23
8	$(\bar{1}11)[211]$	−0.18	**0.47**
9	$(\bar{1}\bar{1}1)[2\bar{1}1]$	−0.01	**0.47**
10	$(1\bar{1}1)[\bar{2}\bar{1}1]$	**0.3**	**0.48**
11	$(111)[\bar{2}11]$	−0.12	**0.48**
12	$(111)[11\bar{2}]$	**0.21**	−0.23

Fig. 1. (a) The stress-strain response of a $[11\bar{1}]_T$ FeMnNiCoCr sample deformed at 77K in tension. The inverse pole figure demonstrates the crystallographic orientation of the undeformed specimen. The schematics showing the activation and migration of the twin systems have been illustrated at different strain levels at points A and B. (b) The high resolution DIC strain contour at the end of the first load increment (D1). The active twin system is identified as $(\bar{1}11)[\bar{1}\bar{2}1]$, which is designated as twin 7 in Table 1. (c) The high resolution DIC strain contour at the end of the third load increment (D3). The active twin system is identified as $(1\bar{1}1)[\bar{2}\bar{1}1]$, which is designated as twin 10 in Table 1. The corresponding twin systems associated with the observed strain bands and their Schmid factors (m) are noted on the contour plots.
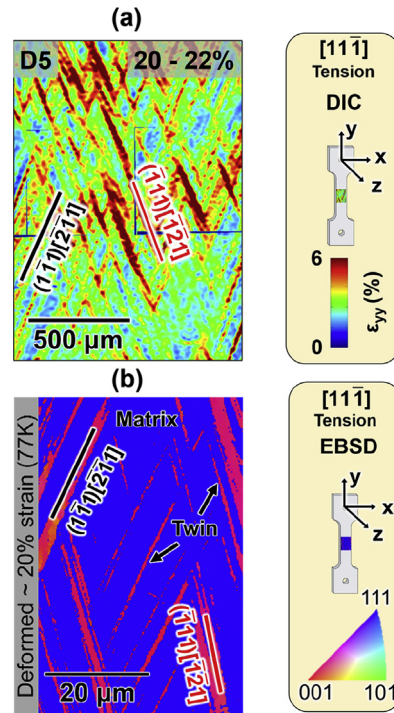
Fig. 2. (a) The high resolution DIC strain contour at D5. (b) The EBSD map taken on the deformed $[11\bar{1}]_T$ FeMnNiCoCr sample with ∼20% strain. Twin formation can be clearly observed displaying a misorientation between matrix and twins of 60°.

3. Experimental results

3.1. The $[11\bar{1}]_T$ tensile case

Fig. 1a shows the stress-strain response for a $[11\bar{1}]_T$ sample deformed in tension at 77K. The stress-strain measures represent true stress and logarithmic strain. The sample was deformed to ∼25% strain in five loading increments and exhibits a Young's modulus of 180 GPa. At the end of the first (D1), third (D3), and fifth (D5) increment, the sample was removed from the load frame for high resolution ex-situ DIC (reference and deformed images captured using the optical microscope). The resulting strain contour plots of the ε_{yy} strains (along loading direction) at D1, D3 and D5 are illustrated in Fig. 1(b) and (c) and 2(a), respectively. In Fig. 1b, at an early stage of deformation, DIC reveals one activated system. Based on trace analysis, the local strain bands coincide with the intersection of the $(\bar{1}11)$ crystallographic plane with the sample's surface. The localized strain bands have been associated with deformation twinning as shown in Fig. 2. The observed twin system is identified as $(\bar{1}11)[\bar{1}\bar{2}1]$ (twin 7) due to its high Schmid factor (0.4). At D3, it is evident that additional localized strain bands corresponding to the $(1\bar{1}1)$ crystallographic plane emerged (at ∼11% strain, see Fig. 1c) which become more pronounced at D5, see Fig. 2a. The strain bands along the $(1\bar{1}1)$ plane have been again attributed to deformation twinning on the $(1\bar{1}1)[\bar{2}\bar{1}1]$ (twin 10) with a Schmid factor of 0.3. The EBSD analysis performed on the deformed sample (∼20% strain) corroborates these results revealing significant twin activities on both $(\bar{1}11)$ and $(1\bar{1}1)$ planes as illustrated in Fig. 2b. Both DIC and EBSD were performed at the center of the gauge section.

Schematics depicting nucleation and migration of twins at points A and B are illustrated in Fig. 1a. At point A, it can be noted that only one twin system nucleated and the hardening slope at this early stage of deformation is about 1 GPa. At point B, with a second system activated, the hardening slope increased to 1.9 GPa introducing an obvious upward shift of the stress-strain response. The increase in the hardening slope when multiple twin systems are activated complies with earlier literature (Efstathiou and Sehitoglu, 2010; Patriarca et al., 2013). This change in the hardening slope is expected to be an outcome of the twin-twin interactions, as will be further elaborated in the discussion. The second twin system has a lower Schmid factor (0.3) compared to the first one (0.4), however its uniaxial nucleation stress (500 ± 10 MPa) is higher than that of the first twin system (410 ± 10 MPa). The nucleation stress was determined as the 0.1% offset stress in case of the first twin system. The nucleation stress of the second system was approximated at Point B where clear strain bands corresponding to the secondary twins were evident according to the ex-situ DIC strain contour plots (see Fig. 1c). In order to calculate the critical resolved shear stress (CRSS) for the second twin system accurately, the crystal orientation was re-measured using EBSD and the Schmid factor was re-established for each twin system based on the new orientation. We note that (based on the Euler angles) the crystal orientation changed from [0.5791 0.4640–0.6703] to [0.5434 0.5257–0.6545]. The corresponding Schmid factor for the $(1\bar{1}1)[\bar{2}\bar{1}1]$ twin system increased from 0.3 to 0.34. The resulting CRSS on the first twin system, $(\bar{1}11)[\bar{1}\bar{2}1]$, is 164 ± 4 MPa and on the second twin system, $(1\bar{1}1)[\bar{2}\bar{1}1]$, 170 ± 3 MPa. To that end, the CRSS of both twin systems are identical within the limits of uncertainty and are in agreement with the Schmid law.
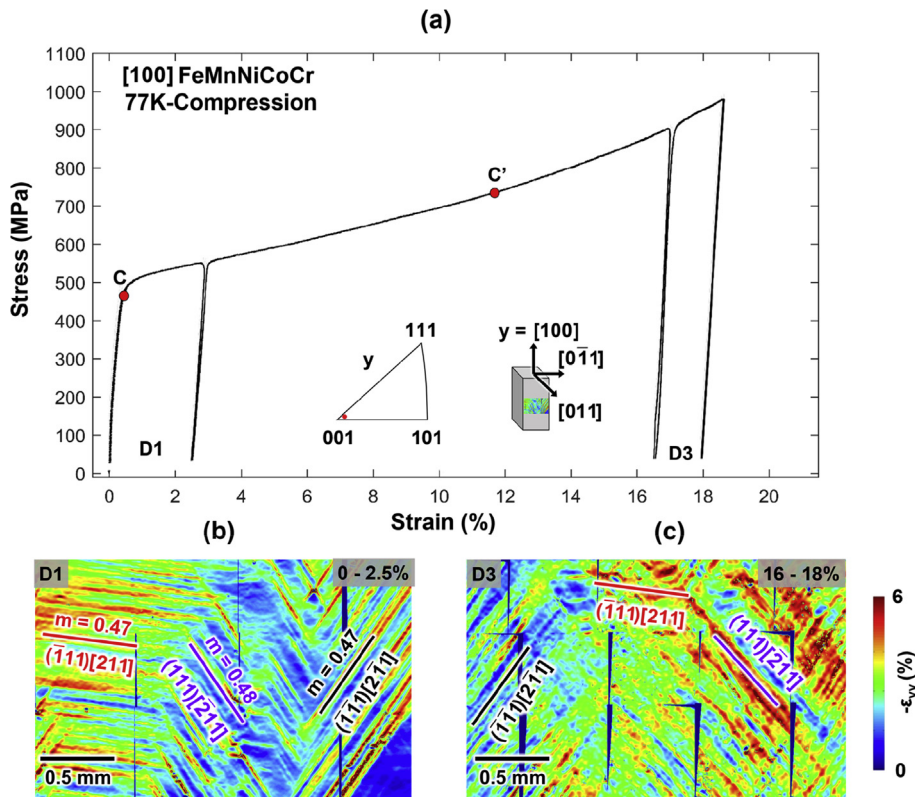
Fig. 3. (a) The stress-strain response of a $[100]_C$ FeMnNiCoCr sample deformed at 77K in compression. The inverse pole figure shows the crystal orientation of the undeformed sample. (b) The high resolution DIC strain contour at the end of the first load increment (D1). The twin systems are identified as $(\bar{1}11)[211]$, $(111)[\bar{2}11]$ and $(\bar{1}\bar{1}1)[2\bar{1}1]$, which correspond to twin 8, 11 and 9 in Table 1. (c) The high resolution DIC strain contour at the end of the third load increment (D3). The corresponding twin systems associated with the observed strain bands and their Schmid factors are noted on the contour plots.

3.2. The $[100]_C$ compressive case

In Fig. 3, the stress-strain behavior of a $[100]_C$ sample tested in compression is presented, its Young's modulus is 112 GPa. High resolution ex-situ DIC strain measurements were performed at the first (D1) and the third (D3) loading increments. The corresponding strain contour plots of the ε_{yy} strain fields are illustrated in Fig. 3(a) and (b). As will be confirmed through TEM analysis in Section 3.3, and EBSD data, the localized slip bands are associated with twinning on three different systems. It is evident that three twin systems were activated at the early stage of deformation (D1 compared to only one system as shown for the $[11\bar{1}]_T$ case. These twins were identified as $(111)[\bar{2}11]$, $(\bar{1}11)[211]$, and $(\bar{1}\bar{1}1)[2\bar{1}1]$ and the corresponding Schmid factors are 0.48, 0.47, and 0.47 respectively. Their nucleation stress, determined at point C with 0.1% offset, is 420 ± 10 MPa, which corresponds to a CRSS level of 197 ± 5 MPa. Compared to the measured CRSS in the $[11\bar{1}]_T$ case, the difference is within 10%. The twin systems observed in the $[100]_C$ case by DIC were also corroborated by the EBSD analysis on the deformed sample (~22% strain). The EBSD map is not presented in this paper for brevity. In addition, the hardening slope of the $[100]_C$ sample is 2.9 GPa, which is approximately 50% higher than that of the $[11\bar{1}]_T$ case (1.9 GPa). The higher hardening slope of the $[100]_C$ case can be related with the increase in the number of active twin systems. We will elaborate more on this point in the discussion.

3.3. TEM analysis

Fig. 4 presents collages of bright-field (BF) TEM and selected area electron diffraction (SAED) patterns of a $[11\bar{1}]_T$ sample deformed to ~20% in tension showing twin-twin and slip-twin/twin-slip interaction. Two active twin systems were observed as evidenced by the SAED. The primary system $(\bar{1}11)[\bar{1}\bar{2}1]$ occupies large parts of the sample and forms very thin to thick twins, from 10 nm up to several 100 nm thick, visible in the upper portion of Fig. 4a. The twinned volumes contain a high density of dislocations in addition to the stacking faults on the $(\bar{1}11)$ twin plane (Fig. 4a). At the center of the image, the secondary twin system $(1\bar{1}1)[\bar{2}\bar{1}1]$ interacts with the primary twin system driving pronounced dislocation emission into the primary twins. Fig. 4b shows a close-up of a secondary twin interacting with the primary twins. While it cuts through the first twin (top Fig. 4b) it is incorporated by the second twin (magnified portion Fig. 4b) as described by the reaction in Table 2.

Fig. 5 shows BF TEM images and SAED patterns of a $[100]_C$ sample deformed to ~25% in compression. By TEM three active twin systems were observed on the $(\bar{1}\bar{1}1)$, $(\bar{1}11)$ and (111) planes. The twins for the $[100]_C$ case having a thickness of several 10 nm are much
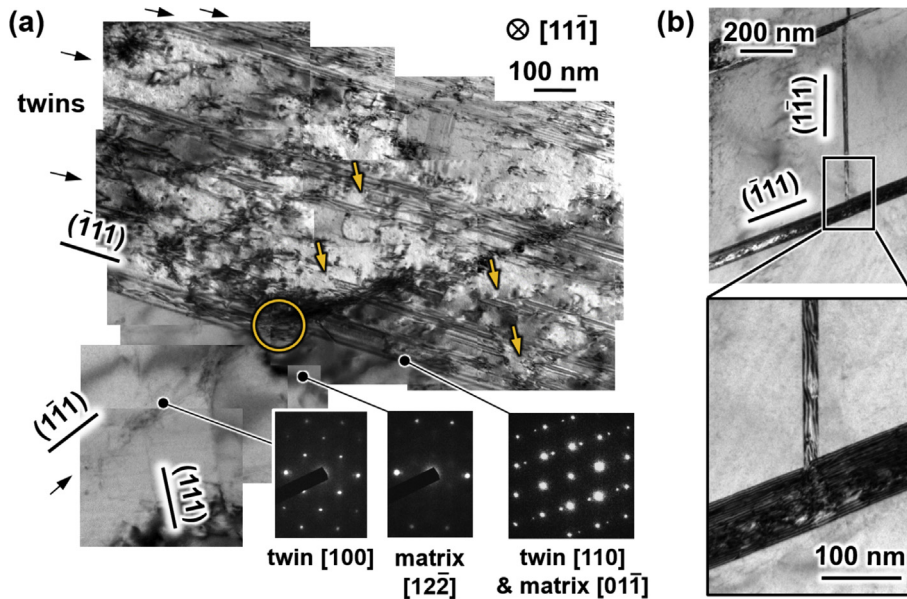
Fig. 4. TEM analysis of a $[11\bar{1}]_T$ tension specimen deformed at 77 K to ~25%. (a) Traces of active planes in the matrix and twins are indicated by black bars and black arrows at the periphery of the collage, respectively. Yellow arrows indicate stacking faults in the twinned area. SAED patterns evidence the formation of two twin variants. Interaction of the $(1\bar{1}1)[\bar{2}\bar{1}1]$ twin with the $(\bar{1}11)[\bar{1}\bar{2}1]$ twin leads to emission of a large number of dislocations into the $(\bar{1}11)[\bar{1}\bar{2}1]$ twins (indicated by the yellow circle). (b) $(1\bar{1}1)[\bar{2}\bar{1}1]$ twin interacting with $(\bar{1}11)[\bar{1}\bar{2}1]$ twins. For presentation purposes (b) has been rotated relative to (a).

finer than those for $[11\bar{1}]_T$ (Fig. 4). In addition to twinning, the aforementioned planes also exhibited pronounced slip activity while the fourth close-packed plane $(1\bar{1}1)$ showed only slip activity without twinning. The higher number of activated systems compared to the $[11\bar{1}]_T$ case leads to more possible interactions, as exemplified in Fig. 5b and c.

Dislocation-based interactions at interfaces, such as twin incorporation (Figs. 4b and 5c), leave behind residual Burgers vectors $\underline{b}^r$ at the interaction site. The residual Burgers vector's magnitude $|\underline{b}^r|$ is indicative for the associated strengthening (Abuzaid et al., 2012). In the next Section 3.4 we show that for incorporation reactions between the twin systems observed the pertaining $|\underline{b}^r|$ values are larger for $[100]_C$ than for $[11\bar{1}]_T$, ultimately leading to higher hardening for $[100]_C$ than for $[11\bar{1}]_T$.

3.4. Residual Burgers vector calculation for twin-twin interactions

The experimental results for the $[11\bar{1}]_T$ and the $[100]_C$ loading cases revealed significant differences in the hardening response. The activation of different twin systems in each of these orientations/loading conditions, which consequently lead to variations in the dislocation reactions during twin-twin interactions, plays a significant role in the observed responses. For example, those reactions resulting in residual dislocations with higher magnitudes (i.e., large residual Burgers vectors), will have higher associated energy barriers, stress levels, and hardening rates compared to interactions proceeding with lower magnitudes of residual dislocation (Chowdhury et al., 2016; Sangid et al., 2012). In order to elucidate the origin of the differences in hardening for the $[100]_C$ vs. the $[11\bar{1}]_T$ orientation we calculate the magnitudes of the residual Burgers vectors $|\underline{b}^r|$ providing insight into the dislocation reactions generated from the observed twin-twin interactions. Based on the TEM analyses shown in Figs. 4b and 5c, we consider the case where the incoming twinning partial gets incorporated into the twin boundary thereby nucleating a twinning partial on the boundary of the barrier twin and leaving behind a residual dislocation Burgers vector ($\underline{b}^r$) at the intersection. The twinning partial formed on the barrier twin boundary is glissile and thus will move under the action of an appropriate resolved shear stress leading to the migration of the barrier twin perpendicular to the twin plane. The glissile twinning partial participates in the migration of the latent twin and

Table 2
Magnitudes of the residual Burgers vectors $|\underline{b}^r|$ for the twin systems observed by DIC and TEM for both $[11\bar{1}]_T$ and $[100]_C$ samples.

Loading direction	Incoming twinning partial ($\underline{b}^{in}$)	Barrier twinning partial ($\underline{b}^{out}$)	Residual Burgers vector ($|\underline{b}^r|$)
$[11\bar{1}]_T$	$3 \times \frac{a}{6}[\bar{2}\bar{1}1]_{T10}$	$\frac{a}{6}[\bar{1}\bar{2}1]_{T7}$	$0.7a$
$[100]_C$	$3 \times \frac{a}{6}[2\bar{1}1]_{T9}$	$\frac{a}{6}[211]_{T8}$	$0.59a$
	$3 \times \frac{a}{6}[2\bar{1}1]_{T9}$	$\frac{a}{6}[\bar{2}11]_{T11}$	$0.94a$
	$3 \times \frac{a}{6}[\bar{2}11]_{T11}$	$\frac{a}{6}[211]_{T8}$	$1.22a$

*$T7$, $T8$, $T9$, $T10$ and $T11$ represents the corresponding coordinate frame of twin systems 7, 8, 9, 10 and 11.
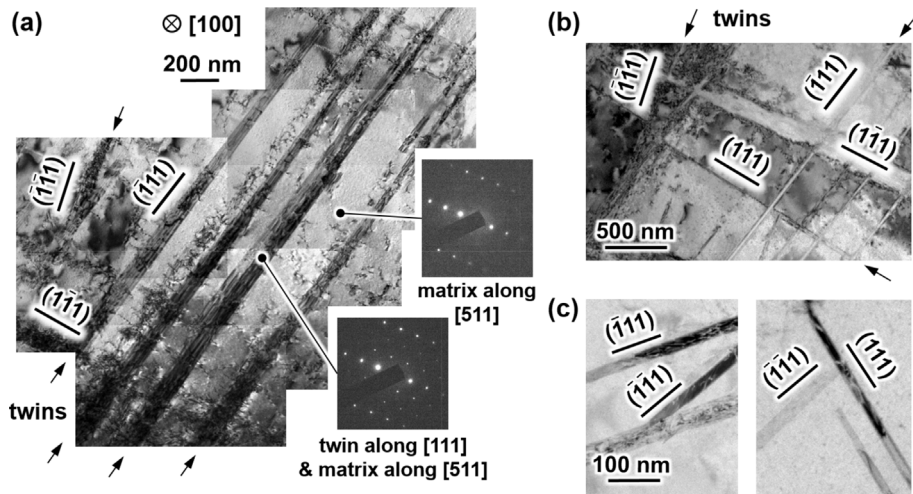
Fig. 5. TEM analysis of a FeMnNiCoCr $[100]_C$ compression sample deformed at 77K to ~25%. (a) Traces of active planes are marked by black bars and SAED patterns evidence twinning on three systems. Black arrows at the periphery of the collage indicate twins. (b) In total, combining twinning and slip four active systems were observed interacting with each other. (c) Incorporation of $(\bar{1}\bar{1}1)[2\bar{1}1]$ twins into $(111)[\bar{2}11]$ and $(\bar{1}11)[211]$ twins. (For presentation purposes (c) has been rotated relative to (a) and (b).).

plays a key role in the strain hardening levels on theoretical grounds. Fig. 6 displays an example from the $[11\bar{1}]_T$ case for the incorporation of incoming twinning partials into the barrier twin boundary as observed by TEM. A select BF image of the interaction site where both incident and barrier twins carry dislocations on their boundaries is shown in Fig. 6a. Images like this demonstrate that the area of intersection (indicated by the circle) contains a high number of dislocations - the residuals left behind by the incorporation reaction. Fig. 6b presents a 3-dimensional model of the dislocation and interface configuration imaged in the TEM micrograph of Fig. 6a, where a primary $(\bar{1}11)[\bar{1}\bar{2}1]$ twin impedes a secondary $(1\bar{1}1)[\bar{2}\bar{1}1]$ twin from growing lengthwise.

The magnitude of the residual Burgers vector $|\underline{b}^r|$ is given by $\underline{b}^{in} = \underline{b}^{out} + \underline{b}^r \Rightarrow |\underline{b}^r| = |\underline{b}^{in} - \underline{b}^{out}|$, where $\underline{b}^{in}$ is the Burgers vector of the incoming Shockley partial and $\underline{b}^{out}$ the Burgers vector of the Shockley partial for the pre-existing barrier twin. The calculation of $|\underline{b}^r|$ needs to be performed in the same coordinate frame. Therefore, in our calculation, $\underline{b}^{out}$ was transformed to the coordinate frame of $\underline{b}^{in}$.

Interacting twin systems can be readily observed from the TEM analysis for $[11\bar{1}]_T$ and $[100]_C$ cases (see Figs. 4 and 5). For ease of discussion, the twin systems were designated according to Table 1 in the following treatment. For example, in the $[100]_C$ sample (see Fig. 5c), the incoming twin system is $(\bar{1}\bar{1}1)[2\bar{1}1]$, which is referred to as twin 9 (T9), while the barrier twin system, $(111)[\bar{2}11]$, is designated as twin 11 (T11, see Table 1). After coordinate transformation, the $[\bar{2}11]$ direction in the coordinate frame of twin 11 (T11) becomes $[2\bar{5}5]$ in the twin 9 (T9) coordinate frame, i.e. $\frac{1}{6}[\bar{2}11]_{T11} = \frac{1}{18}[2\bar{5}5]_{T9}$. According to the earlier literature (Mahajan and Chin, 1973, 1974; Remy, 1977, 1981), it is necessary to incorporate triplets of incident twin dislocations to obtain steps of integral multiples of the inter-planar distance for {111} planes at the interface of the barrier twin. Therefore, in the coordinate frame of T9, the dislocation reaction can be expressed as $3 \times \frac{a}{6}[2\bar{1}1] = \frac{a}{18}[2\bar{5}5] + \underline{b}^r \Rightarrow |\underline{b}^r| = 0.94a$, where a is the lattice constant. The
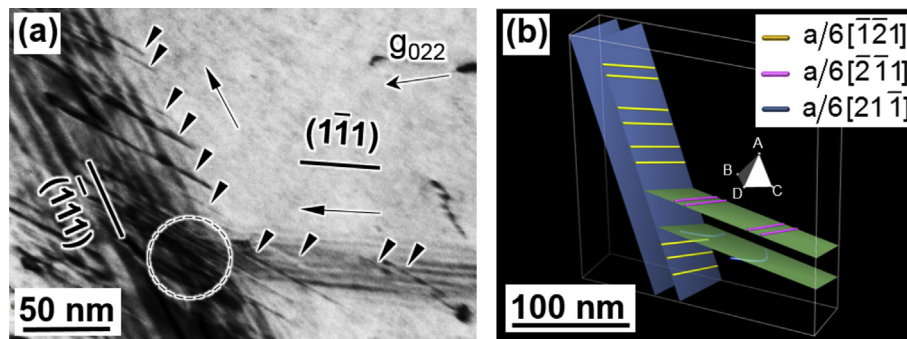
Fig. 6. (a) A two-beam BF image of the interaction site of a secondary $(1\bar{1}1)[\bar{2}\bar{1}1]$ twin with a primary $(\bar{1}11)[\bar{1}\bar{2}1]$ twin in a $[11\bar{1}]_T$ specimen. Several twinning dislocations, marked by arrowheads, are present on the twin boundaries. Their assumed direction of movement is indicated by arrows. The area marked by the circle contains a high strain density from residual dislocations. The (022) reflection of the matrix crystal was tilted into the two-beam condition to obtain the image. (b) A model of the interaction site constructed from a series of tilted images such as in (a) illustrating the 3-dimensional arrangement of dislocations and interfaces around the interaction site. The high dislocation density in the region marked by the circle prevented the reconstruction of the exact dislocation arrangement therein. The Thompson tetrahedron (following the notation in (Hirth, 1961)) shows the coordinate system of the matrix; dislocations are color coded according to their Burgers vectors; blue and green planes correspond to twin planes of the primary and the secondary system, respectively.

corresponding $|\underline{b}^r|$ of all possible twin-twin interactions (incorporation) are tabulated in Table 2. Inverting the reaction direction by replacing the incoming with the barrier twin system and vice versa leads to similar $|\underline{b}^r|$. Note that $|\underline{b}^r|$ for the $[11\bar{1}]_T$ sample is lower than for the interactions in the $[100]_C$ sample except where twin 8 interacts with twin 9. The lower $|\underline{b}^r|$ for $[11\bar{1}]_T$ is consistent with its lower hardening rate relative to $[100]_C$. This observation once again strengthens the notion that $|\underline{b}^r|$ is directly related to the degree of strengthening attendant to dislocation reactions at intersecting interfaces.

3.5. Calculation of the latent hardening moduli

It has been well-established that there are four different mechanisms that can contribute to the overall hardening of a single crystalline material, slip-slip, slip-twin, twin-slip and twin-twin interactions (Friedel, 1955; Jin et al., 2008; Mahajan and Chin, 1973, 1974; Patriarca et al., 2013; Remy, 1977, 1981). For a proper understanding of the hardening response, the contribution from each of these four different mechanisms has to be evaluated. As discussed previously, the different hardening moduli $h_{\alpha'\beta'}^{slip-slip}$, $h_{\alpha'\beta'}^{slip-twin}$, $h_{\alpha\beta}^{twin-slip}$ and $h_{\alpha\beta}^{twin-twin}$ have been used to capture the separate contribution from each of the possible reactions contributing to the strengthening of the single crystal. In this section, we focus on acquiring the $h_{\alpha\beta}$ values associated with twin-twin interactions, since they dominate the hardening as we will demonstrate. Based on the post-mortem TEM and EBSD analysis (Figs. 2b, 4b and 5c), it is evident that the twin activities dominate the deformed microstructures, warranting to assume that plastic deformation of both $[11\bar{1}]_T$ and $[100]_C$ FeMnNiCoCr single crystals is mainly accommodated by twin activities. As for the contribution due to slip-slip, slip-twin and twin-slip interactions, the associated $h_{\alpha\beta}$ values can be determined based on the previous study by Abuzaid and Sehitoglu (2017). The corresponding calculation procedures and results are shown in the Appendix B.

The moduli of self hardening ($h_{\alpha\alpha}^{twin-twin}$) and latent hardening $h_{\alpha\beta}^{twin-twin}$ ($\alpha \neq \beta$) due to twin-twin interactions were calculated for both $[11\bar{1}]_T$ and $[100]_C$ cases using the constitutive equation (Equation (2)). We confirmed 2 systems nucleated for the $[11\bar{1}]_T$ sample and 3 systems for the $[100]_C$ sample based on DIC and TEM analysis. In the $[11\bar{1}]_T$ case, the systems were activated consecutively (see Fig. 1), where a primary twin system was initiated at the early stage of deformation and nucleation of a secondary system ensued at higher strains. We calculated $h_{\alpha\alpha}^{twin-twin}$ and $h_{\alpha\beta}^{twin-twin}$ ($\alpha \neq \beta$) associated with the $[11\bar{1}]_T$ loading case when both the primary and latent systems are present (B to B′ in Fig. 1a). $h_{\alpha\beta}^{twin-twin}$ of the $[100]_C$ sample was also calculated from C to C′ using Equation (2). Since nucleation of all three twin systems occurred simultaneously, several assumptions have to be proposed in order to facilitate the calculation. In the following sections, we will elaborate on the procedures we established to obtain the $h_{\alpha\beta}$ values for both $[11\bar{1}]_T$ and $[100]_C$ cases.

3.5.1. The $[11\bar{1}]_T$ loading case

For $[11\bar{1}]_T$ the range B to B′ (shown in Fig. 1a) uncovered a clear interaction between the primary twin system 7 and the latent twin system 10 permitting to extract the strain hardening moduli for these two systems. Adapting Equation (2) for this particular case, the correlation between the increase of shear stress and the shear strain increment can be expressed as follows,

$$d\tau_{critical}^{(7)} = h_{77}^{twin-twin} df_{twin}^{(7)} \gamma_{twin}^{fcc} + h_{710}^{twin-twin} df_{twin}^{(10)} \gamma_{twin}^{fcc} \tag{3a}$$

$$d\tau_{critical}^{(10)} = h_{107}^{twin-twin} df_{twin}^{(7)} \gamma_{twin}^{fcc} + h_{1010}^{twin-twin} df_{twin}^{(10)} \gamma_{twin}^{fcc} \tag{3b}$$

where $h_{107}^{twin-twin}$ and $h_{710}^{twin-twin}$ are the terms governing the latent hardening response due to the interaction between twin 7 and twin 10 and $h_{77}^{twin-twin}$ and $h_{1010}^{twin-twin}$ are the twin self hardening moduli. We defined that, in the case of twin-twin interaction, the off-diagonal terms can be related to the diagonal terms with a proportionality parameter q, which is also analogous to what has been employed in the slip case (Brahme et al., 2011; Peirce et al., 1982; Wu et al., 1991). The magnitude of q associated with different twin-twin interactions is expected to be different. In this section, we demonstrate the calculation for the q value associated with the interaction between twin 7 and twin 10. Inspired by the framework of the slip-induced latent hardening response proposed by Wu et al. (1991), the relationship between the two self hardening moduli can be expressed as follows,

$$\frac{h_{1010}^{twin-twin}}{h_{77}^{twin-twin}} \approx \Gamma M \tag{4}$$

where Γ is the ratio between the shear strain increment associated with twin 7 and twin 10, i.e. $d\gamma_{twin}^{(7)}/d\gamma_{twin}^{(10)} \sim 1.35$, and M is the ratio between the Schmid factors of the twin systems. After integrating Equation (2) from B to B′ with Equation (4) incorporated, the following expressions can be obtained,

$$\int_{m^{(7)}\sigma_B}^{m^{(7)}\sigma_{B'}} d\tau_{critical}^{(7)} = \gamma_{twin}^{fcc} \int_{f_B^{(7)}}^{f_{B'}^{(7)}} h_{77}^{twin-twin} df_{twin}^{(7)} + q\Gamma M \gamma_{twin}^{fcc} \int_{f_B^{(10)}}^{f_{B'}^{(10)}} h_{77}^{twin-twin} df_{twin}^{(10)} \tag{5a}$$

$$\int_{m^{(10)}\sigma_B}^{m^{(10)}\sigma_{B'}} d\tau_{critical}^{(10)} = q\gamma_{twin}^{fcc} \int_{f_B^{(7)}}^{f_{B'}^{(7)}} h_{77}^{twin-twin} df_{twin}^{(7)} + \Gamma M \gamma_{twin}^{fcc} \int_{f_B^{(10)}}^{f_{B'}^{(10)}} h_{77}^{twin-twin} df_{twin}^{(10)} \tag{5b}$$

where $f_{B'}^{(7)}$, $f_B^{(7)}$, $f_{B'}^{(10)}$ and $f_B^{(10)}$ represent the volume fractions of twin 7 at point B′ and point B and twin 10 at point B′ and point B, respectively. We designated that the hardening moduli are constant at the considered strain level. It is necessary to solve for q and $h_{77}^{twin-twin}$ in order to establish the latent hardening terms. The stress levels at point B and point B′ are taken as $\sigma_{B'}$ = 650 MPa and σ_B = 575 MPa (see Fig. 1). We estimated the volume fractions of the observed twin systems based on the ex-situ DIC strain contours.
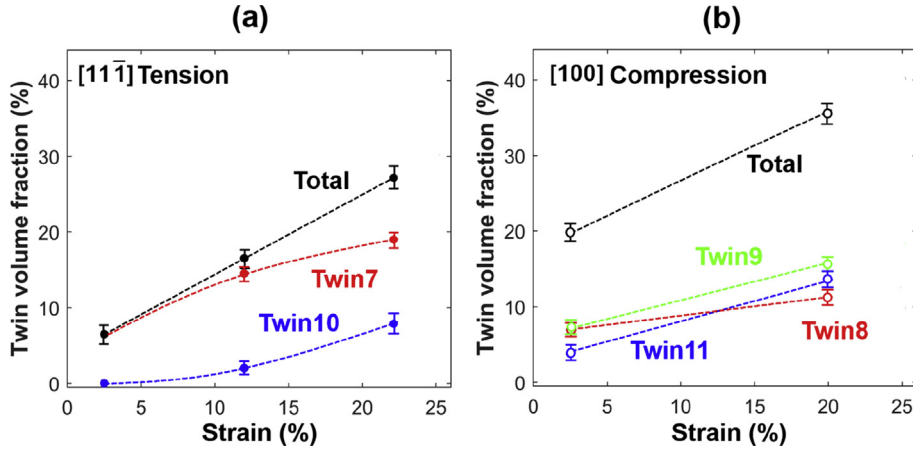
Fig. 7. The evolution of volume fraction of each twin system as a function of strain. The dashed lines are added to aid the eyes.

Each localized strain band represents a certain amount of volume fraction of twinning. The total volume fraction was inferred from the areal fraction of the localized strain bands over the entire gauge section (~ 3 mm $\times$ 10 mm). Fig. 7 illustrates the evolution of the twin volume fraction as a function of strain for all observed twin systems for $[11\bar{1}]_T$ and $[100]_C$. From Fig. 7a, we can approximate the volume fractions of twin 7 and twin 10 as $f_{B'}^{(7)} \sim 14.5\%$, $f_{B'}^{(10)} \sim 2\%$, $f_B^{(7)} \sim 11.5\%$ and $f_B^{(10)} \sim 0\%$. Due to the strong plastic deformation, the crystal orientation was re-measured at point B using EBSD. The corresponding Schmid factors of twin 7 and twin 10 were re-calculated as $m^{(7)} = 0.38$ and $m^{(10)} = 0.34$. Solving Equations (6a) and (6b), the unknowns are calculated as $q = 0.32$ and $h_{77}^{twin-twin} = 1.17$ GPa. Using Equation (4), $h_{1010}^{twin-twin}$ can be determined from $h_{77}^{twin-twin}$ as 1.29 GPa. Consequently, the latent hardening terms are $h_{710}^{twin-twin} = 0.40$ GPa and $h_{107}^{twin-twin} = 0.37$ GPa. Note that $h_{710}^{twin-twin} \sim h_{107}^{twin-twin}$, which also complies with earlier reports where symmetry of the $\{h_{\alpha\beta}\}$ matrix is often assumed (Asaro, 1983; Hutchinson, 1970; Peirce et al., 1982).

3.5.2. The $[100]_C$ loading case

In the $[100]_C$ sample, three twin systems were activated at the early stage of deformation (see Fig. 3b). The flow stress increment for each system can be expressed as the following,

$$d\tau_{critical}^{(8)} = h_{88}^{twin-twin} df_{twin}^{(8)} \gamma_{twin}^{fcc} + h_{89}^{twin-twin} df_{twin}^{(9)} \gamma_{twin}^{fcc} + h_{811}^{twin-twin} df_{twin}^{(11)} \gamma_{twin}^{fcc} \tag{6a}$$

$$d\tau_{critical}^{(9)} = h_{98}^{twin-twin} df_{twin}^{(8)} \gamma_{twin}^{fcc} + h_{99}^{twin-twin} df_{twin}^{(9)} \gamma_{twin}^{fcc} + h_{911}^{twin-twin} df_{twin}^{(11)} \gamma_{twin}^{fcc} \tag{6b}$$

$$d\tau_{critical}^{(11)} = h_{118}^{twin-twin} df_{twin}^{(8)} \gamma_{twin}^{fcc} + h_{119}^{twin-twin} df_{twin}^{(9)} \gamma_{twin}^{fcc} + h_{1111}^{twin-twin} df_{twin}^{(11)} \gamma_{twin}^{fcc} \tag{6c}$$

As expected, the latent hardening description becomes increasingly complex as the number of systems increase and a satisfactory methodology to establish all constants is rather difficult. Since we have 6 unknowns and 3 equations, several assumptions were made in order to facilitate the calculation, as justified below. In this work, we focus on the latent hardening terms ($h_{89}^{twin-twin}$, $h_{118}^{twin-twin}$ and $h_{119}^{twin-twin}$) which can give insight into the latent hardening response of the material due to twin-twin interactions. As all 12 {111} <112> fcc twinning systems are crystallographically equivalent, we expect the diagonal terms, $h_{88}^{twin-twin}$, $h_{99}^{twin-twin}$, and $h_{1111}^{twin-twin}$, to be identical in value and equal to the average of $h_{77}^{twin-twin}$ and $h_{1010}^{twin-twin}$ calculated for the $[11\bar{1}]_T$ case. Furthermore, we assume that the hardening matrix $\{h_{\alpha\beta}^{twin-twin}\}$ is symmetric, i.e. $h_{89}^{twin-twin} = h_{98}^{twin-twin}$, $h_{118}^{twin-twin} = h_{811}^{twin-twin}$ and $h_{119}^{twin-twin} = h_{911}^{twin-twin}$. Under these circumstances, the calculation of the corresponding hardening coefficients can be accomplished as the number of the linearly-independent equations and unknowns are equal, i.e. 3. After integration, Equations (6a), (6b) and (6c) become the following,

$$\int_{m^{(8)}\sigma_C}^{m^{(8)}\sigma_{C'}} d\tau_{critical}^{(8)} = \gamma_{twin}^{fcc} \int_0^{f_{C'}^{(8)}} h_{88}^{twin-twin} df_{twin}^{(8)} + \gamma_{twin}^{fcc} \int_0^{f_{C'}^{(9)}} h_{89}^{twin-twin} df_{twin}^{(9)} + \gamma_{twin}^{fcc} \int_0^{f_{C'}^{(11)}} h_{811}^{twin-twin} df_{twin}^{(11)} \tag{7a}$$

$$\int_{m^{(9)}\sigma_C}^{m^{(9)}\sigma_{C'}} d\tau_{critical}^{(9)} = \gamma_{twin}^{fcc} \int_0^{f_{C'}^{(8)}} h_{98}^{twin-twin} df_{twin}^{(8)} + \gamma_{twin}^{fcc} \int_0^{f_{C'}^{(9)}} h_{99}^{twin-twin} df_{twin}^{(9)} + \gamma_{twin}^{fcc} \int_0^{f_{C'}^{(11)}} h_{911}^{twin-twin} df_{twin}^{(11)} \tag{7b}$$

$$\int_{m^{(11)}\sigma_C}^{m^{(11)}\sigma_{C'}} d\tau_{critical}^{(11)} = \gamma_{twin}^{fcc} \int_0^{f_{C'}^{(8)}} h_{118}^{twin-twin} df_{twin}^{(8)} + \gamma_{twin}^{fcc} \int_0^{f_{C'}^{(9)}} h_{119}^{twin-twin} df_{twin}^{(9)} + \gamma_{twin}^{fcc} \int_0^{f_{C'}^{(11)}} h_{1111}^{twin-twin} df_{twin}^{(11)} \tag{7c}$$

The experimental data, $\sigma_{C'}$ (~ 720 MPa), $f_{C'}^{(8)}$ ($\sim 8.9\%$), $f_{C'}^{(9)}$ ($\sim 11.7\%$) and $f_{C'}^{(11)}$ ($\sim 6.1\%$) are extracted at point C' from the stress-strain curve of the $[100]_C$ sample (see Fig. 3). By solving Equations (7a), (7b) and (7c), the latent hardening terms are obtained as $h_{89}^{twin-twin} = 0.32$ GPa, $h_{119}^{twin-twin} = 0.44$ GPa and $h_{118}^{twin-twin} = 0.86$ GPa. We summarize the self hardening and latent hardening moduli computed based on the experimental measurements for the observed twin-twin interactions in Table 3. These results are also in line with the theoretcial predictions (Alkan et al., 2018). It is evident that the latent hardening moduli ($h_{89}^{twin-twin}$, $h_{107}^{twin-twin}$, $h_{119}^{twin-twin}$ and $h_{118}^{twin-twin}$) are smaller than the self hardening moduli, which is consistent with the result found by Wu et al. (1991). Close examination

Table 3
The $h_{\alpha\beta}$ values for different twin interactions determined from the experiments.

		$h_{\alpha\beta}$ (GPa)	$|\underline{b}^r|$
Self hardening	$h_{77}^{twin-twin}$ [a]	1.17	–
	$h_{1010}^{twin-twin}$ [a]	1.29	–
Latent Hardening	$h_{89}^{twin-twin}$ [b]	0.32	0.59a
	$h_{107}^{twin-twin}$ [a]	0.37	0.70a
	$h_{119}^{twin-twin}$ [b]	0.44	0.94a
	$h_{118}^{twin-twin}$ [b]	0.86	1.22a

[a] Determined from the $[11\bar{1}]_T$ loading case.
[b] Determined from the $[100]_C$ loading case.

of the $|\underline{b}^r|$ value (see Table 2) in comparison with $h_{\alpha\beta}$ ($\alpha \neq \beta$), shows that when the $|\underline{b}^r|$ value is the highest, i.e. 1.22a, the corresponding latent hardening moduli culminate among all possible reactions, i.e. $h_{118}^{twin-twin}$ = 0.81 GPa. This result also infers a possible correlation between $|\underline{b}^r|$ and $h_{\alpha\beta}$ ($\alpha \neq \beta$).

3.5.3. Insight into the self hardening modulus of isolated twinning

It is feasible to obtain the self hardening modulus of isolated twinning (single twin system active without prior slip or twin activity on other systems) at the early stage of deformation (A to A', see Fig. 1a) in the $[11\bar{1}]_T$ case. Fig. 1b demonstrates that the total plastic strain was accommodated by only one twin system (twin 7) in the $[11\bar{1}]_T$ case. Since we acquired similar CRSS values for twin 7 and twin 10 at point A and point B, respectively, it is fair to assume that no latent hardening has occurred from A to B. Consequently, the hardening can be expressed as follows,

$$d\tau_{critical}^{(7)} = h_{77}^{iso} df_{twin}^{(7)} \gamma_{twin}^{fcc} \tag{8}$$

where h_{77}^{iso} is the self hardening modulus of the isolated twin system 7. After integration, Equation (8) becomes the following,

$$\int_{m^{(7)}\sigma_A}^{m^{(7)}\sigma_{A'}} d\tau_{critical}^{(7)} = \gamma_{twin}^{fcc} \int_0^{f_{A'}^{(7)}} h_{77}^{iso} df_{twin}^{(7)} \tag{9}$$

where $m^{(7)}$ is the Schmid factor of twin 7, and $f_{A'}^{(7)}$ is the volume fraction of twin 7. The calculation of h_{77}^{iso} was performed at the end of the loading process of strain increment D1 (see point A' in Fig. 1) where $\sigma_{A'}$ is 445 MPa (prior to unloading). Then, the shear strain was approximated as $f_{A'}^{(7)} \gamma_{twin}$ = 7.4% × 0.707 = 5.2% for point A' in Fig. 1a. Using these experimental results for $[11\bar{1}]_T$ and Equation (9), we can derive an estimate of the self hardening modulus for an isolated twin system as h_{77}^{iso} = 0.15 GPa. This value is almost ten times smaller than the one obtained from the case where both primary and latent systems are present, i.e. $h_{77}^{twin-twin}$ = 1.1 GPa.

4. Discussion

4.1. Hardening anisotropy

The stress-strain responses for the two favorable twinning orientations, $[11\bar{1}]_T$ and $[100]_C$, revealed a dissimilar hardening response (i.e., slope $d\sigma/d\varepsilon$). It is evident that the strain hardening response of FeMnNiCoCr single crystals is orientation dependent, for the $[100]_C$ sample $d\sigma/d\varepsilon$ = 2.9 GPa compared to the $[11\bar{1}]_T$ sample $d\sigma/d\varepsilon$ = 1.9 GPa. We offer the following rationale based on our experimental observations. There are two interrelated factors that can affect the strain hardening coefficient: the magnitude of the residual Burgers vector due to twin-twin interaction and the number of activated twin systems. As shown in Table 2, the magnitude of the residual Burgers vector is higher in the $[100]_C$ case compared to the $[11\bar{1}]_T$ for most of the observed interactions. Especially, the interaction between twin 11 and twin 8 in the $[100]_C$ case produces the highest $|\underline{b}^r|$ = 1.22a among all possible reactions. In addition, 3 twin systems nucleated in the $[100]_C$ case compared to 2 in the $[11\bar{1}]_T$ case. Mutual interactions of multiple twin systems in the $[100]_C$ loading case can further enhance the strain hardening level (Efstathiou and Sehitoglu, 2010). Based on these observations, the orientation dependency of the strain hardening response of single-crystalline FeMnNiCoCr can be attributed conclusively to the combined effect of: (i) differences in the magnitude of the residual Burgers vectors, $|\underline{b}^r|$, formed by twin-twin interactions and (ii) the differing number of active twin systems for different loading directions.

The extent of strengthening in a latent system can be characterized by its corresponding latent hardening modulus. A higher $h_{\alpha\beta}$ ($\alpha \neq \beta$) value implies that the strengthening of the latent system due to the deformation of the primary system is more pronounced. Although the determination of the latent hardening moduli on experimental grounds for the case where two systems are activated is feasible, it is a formidable task for higher number of systems. In this study, we assumed the symmetry of the hardening matrices $\{h_{\alpha\beta}^{slip-slip}\}$ and $\{h_{\alpha\beta}^{twin-twin}\}$ (Section 3.5) and isotropic self hardening of the twin systems (identical $h_{\alpha\alpha}^{twin-twin}$ values) in order to facilitate the calculation process. When comparing the latent hardening moduli of the $[11\bar{1}]_T$ with the $[100]_C$ sample, we note that the strengthening of the latent twin system is more significant in the $[100]_C$ case as its $h_{\alpha\beta}^{twin-twin}$ ($\alpha \neq \beta$) values are shifted to higher values relative to those for $[11\bar{1}]_T$ (see Table 3). Especially, for the case where interaction between twin 11 and twin 8 occurred in the $[100]_C$ sample, the corresponding latent hardening modulus is the highest ($h_{118}^{twin-twin}$ = 0.81 GPa). This analysis shows that the remarkable

strain hardening response of the $[100]_C$ loading case can also be correlated with the increased strengthening of the latent twin systems during deformation in addition to higher number of active twins and higher $|\underline{b}^r|$.

4.2. The uniqueness of our latent hardening determination approach

It is important to reiterate that the latent hardening response of the FeMnNiCoCr HEA was investigated under a different scenario in this work compared to latent hardening studies of other materials in earlier literature. For previous undertakings (Franciosi, 1983, 1985; Franciosi et al., 1980; Jackson and Basinski, 1967; Kocks and Brown, 1966; Nakada and Keh, 1966), deformation was performed in two steps whereby during the first a single primary system was initiated. Nucleation of latent slip systems in the second step was achieved by re-orienting the pre-deformed single crystals at angles where the primary system becomes inactive, leaving only previously latent systems active. From such tests the hardening of previously inactive secondary systems was assessed by the latent hardening ratio (LHR) which relates the CRSS on the second system to the maximal stress on the primary system during the first step. This testing route is an idealized set-up which has proven very instructive. However, it is important to note that the deformation often proceeds continuously in a monotonic fashion in more application relevant settings. In the present study, the crystal was deformed continuously so that a system, once initiated, remained active throughout the test. The rotation of the loading orientation after deformation is approximately 2°. The orientation changes were accounted in the modified Schmid factors as outlined in Appendix C. The newly established procedure in this work allows the study of self and latent hardening under realistic loading conditions eliminating the need of sample re-orientation which, as discussed previously, aims to suppress the primary system. This has been made possible through the utilization of EBSD and high resolution DIC data. The full field strain measurements enabled relatively simple assessment of the number of activated twin systems (i.e., localized strain bands observed in DIC contour plots) which can be indexed using EBSD. With such data collected at two different loading levels, the twin volume fraction for each of the activated systems becomes available and allows extraction of the hardening moduli. Such a construction of the $h_{\alpha\beta}$ values based on proportional experiments resulted in self hardening magnitudes exceeding the latent hardening in a number of cases as we elaborate below.

Early studies on slip-slip interactions invariably reported a latent hardening of the secondary system larger than the self hardening of the primary system independent of test temperature (Franciosi, 1983, 1985; Franciosi et al., 1980; Jackson and Basinski, 1967; Kocks and Brown, 1966; Nakada and Keh, 1966), seemingly conflicting with our analysis though conclusively resolvable bearing the particular experimental methodologies utilized in these studies vs. the present in mind. Table 4 presents an overview of the pertaining LHRs for cubic materials in comparison with the LHR values calculated from the hardening moduli obtained in the present study based on Equation (10) (Franciosi et al., 1980),

$$\text{LHR}_{ij} = \frac{\tau_0^i + h_{latent}^{ij} \cdot \gamma^j}{\tau_0^j + h_{self}^{ij} \cdot \gamma^j}$$

(10)

where τ_0^i and τ_0^j denote the CRSS for the latent and primary system, respectively, γ^j is the shear strain of the primary system, and i and j indicate slip or twinning (no summation of identical indices). Utilizing the average CRSS for slip ($\tau_0^{slip} = 153$ MPa(Abuzaid and Sehitoglu, 2017)) and twin nucleation ($\tau_0^{twin} = 177$ MPa) combined with the average self and latent hardening modulus for each interaction type given in Equation (11) (excluding the self hardening moduli for isolated slip and isolated twinning),

$$
\begin{bmatrix}
h_{self}^{slip-slip} \\
h_{latent}^{slip-slip} \\
h_{latent}^{twin-slip} \\
h_{latent}^{slip-twin} \\
h_{self}^{twin-twin} \\
h_{latent}^{twin-twin}
\end{bmatrix}
=
\begin{bmatrix}
0.023 \\
0.012 \\
0.055 \\
0.042 \\
1.225 \\
0.468
\end{bmatrix}
\text{GPa}
$$

(11)

the dependence of LHR on primary shear strain is depicted in Fig. 8 for all four interactions types (slip-slip, twin-slip, slip-twin and twin-twin) that occur in FeMnNiCoCr single crystals. These curves were obtained under the premise that the hardening moduli in Equation (11) (which were determined at a strain level of ~10%) are independent of the amount of primary shear strain γ^j. To test the validity of this assumption, the self and latent hardening moduli were additionally extracted from the stress-strain curves for strains of ~5% for twin-twin ($[11\bar{1}]_T$ and $[100]_C$ samples, Figs. 1 and 3) and for slip-slip ($[\bar{1}49]_T$ sample, Fig. A1) interactions. The resulting hardening moduli exhibited only minor changes. Consequently, the LHRs for 10% of strain (shown by solid lines in Fig. 8) do not differ from those for 5% of strain (indicated by crosses).

Fig. 8 demonstrates that LHR depends sensitively on the interaction type. For example, the LHR is approximately 1.17 for twin-slip and is less than 1 for the other interaction types (slip-slip, twin-twin, and slip-twin). Furthermore, for twin-twin and slip-twin interactions, LHR decreases considerably below 1 with the amount of strain on the primary system γ^j, also for moderate $\gamma^j < 0.1$, as shown in Fig. 8 and Table 4.

LHRs for slip-slip interactions in cubic materials have almost invariably been reported to be > 1 both at room temperature (RT) and cryogenic temperature (77K), in some cases reaching values as high as 3.9 depending on the primary shear strain γ^j, (Table 4). Yet, it has to be kept in mind that these studies determined the CRSS for the secondary system by back-extrapolation of the flow stress which may lead in some cases to a considerable overestimation of the true critical stress given by the first deviation from the linear

Table 4

Experimentally determined latent hardening ratios (LHRs) and q^{ij} values for cubic single crystalline materials from the literature in comparison with those from the present work.

Investigators	Material	Interaction	LHR	Primary shear strain (%)	q^{ij}	Temperature, Orientation	Comments
Kocks and Brown (Kocks and Brown, 1966)	Al, fcc	slip-slip	1.15–1.4	~12	1.3–1.5	RT, various	†,°, non-coplanar
			0.95–1.15	~12	0.9–1.1		†,°, coplanar
Jackson and Basinski (Jackson and Basinski, 1967)	Cu, fcc	slip-slip	1.3–2.6	2–24	1.4–5.6	RT, various	†,°,*, non-coplanar
			~1		~1		†,°, coplanar
Franciosi, Berveiller and Zaoui (Franciosi et al., 1980)	Al, fcc	slip-slip	1.3–2.3	0–0.8	1.1–2.8	RT, various	†,°,*
	Cu, fcc	slip-slip	1.4–3.9	0.2–2.7	1.3–5.8		†,°,*
Franciosi (Franciosi, 1985)	Ag, fcc	slip-slip	2.25–3.7	0.7–0.85	–	RT, various	†,°,*
	Cu-4%Zn, fcc	slip-slip	0.5–2.2	0.4–2.8	–		†,°
Wessels and Jackson (Wessels and Jackson, 1969)	Cu-(0.5–10)%Al, fcc	slip-slip	1.32–2.53	–	–	RT, various	†,°
Wessels and Nabarro (Wessels and Nabarro, 1971)	Cu-5%Al, fcc	slip-slip	1.2–2.45	–	–	RT, various	†,°, non-coplanar
			0.9–1.25	–	–		†,°, coplanar
			1.6–1.8	–	–	77K, various	†,°, non-coplanar
Wu, Bassani and Laird (Wu et al., 1991)	Cu, fcc	slip-slip	0.6–1.1	1.2–2	0.1–1.3	RT, various	†, CRSS of latent system determined by first deviation from linearity
Franciosi (Franciosi, 1983)	α-Fe, bcc	slip-slip	1.05–1.85	0.8–1.65	1.1–3.2	RT, various	†,°,*
Nakada and Keh (Nakada and Keh, 1966)	α-Fe, bcc	slip-slip	1.2–1.4	10.7–27	1.4–3.2	RT, various	†,°,*
			1.28	11	–	77K, various	†,°
This work	FeCoCrMnNi, fcc	slip-slip	~1	0–10	0.51	77K, $[\bar{1}49]_T$	◇
		twin-slip	~1.17	0–10	2.44	77K, $[21\bar{2}]_T$	◇, primary slip, secondary twinning
		slip-twin	0.54–0.84	0–10	0.04	77K, $[21\bar{2}]_T$	◇, primary twinning, secondary slip
		twin-twin	0.77–1	0–10	0.41	77K, $[100]_C,[11\bar{1}]_T$	◇

†… 2-step incremental procedure with reorientation of loading axis between first segment (primary slip) and second segment (activation of latent system).

°… CRSS of latent system determined by back-extrapolation.

* … LHR peaks and then decreases to value > 1 with increasing shear strain on primary system.

◇ … continuous loading, CRSS for slip τ_0^{slip} = 153 MPa, CRSS for twinning τ_0^{slip} = 177 MPa.

elastic regime. Wu et al. (1991) showed that when the CRSS of the secondary system is deducted from the first deviation from linearity LHRs smaller than unity (representing a weaker latent than self hardening) are obtained, in line with the present results.

While the LHR defined in Equation (10) is affected by the CRSSs of both primary (τ_0^j) and secondary (τ_0^i) systems, the ratio of the latent to self hardening moduli/slopes

$$q^{ij} = \frac{h_{latent}^{ij}}{h_{self}^{jj}}$$

(12)

reflects more closely the intrinsic difference between hardening on the primary and the secondary system upon straining the primary system. In Table 4 we list the values for q^{ij} based on our data and those from literature. While Kocks (1970) suggested $q^{slip-slip} \sim 1.4$ (past easy glide), our analysis (both of literature data and of our own results) demonstrates a broad range for $q^{slip-slip}$ from 0.1 to 5.8 reflecting the sensitivity of the hardening response to the interaction type, active systems, residual Burgers vectors, amount of primary strain and to variations in the material intrinsic properties at the atomic scale. The large scatter of q^{ij} values attests the necessity to scrutinize each interaction type separately in carefully devised experiments or numerical simulation frameworks incorporating the individual and combined effects of the factors mentioned above.

Our results show that the q^{ij} values for interactions involving twinning and slip range from 0.04 for slip-twin to 2.44 for twin-slip and pure interactions (slip-slip, twin-twin) lie between these values. Among all types of interactions, the latent system hardens faster than the active only for twin-slip (primary slip, secondary twinning); for the other cases the opposite is found: the active system hardens faster than the latent ones.

It is worth recalling that in our $[11\bar{1}]_T$ case the primary and the secondary twins nucleated at the same resolved shear stress albeit at different strains (and stress). In other words, the latent twin system was not hardened by prior isolated activity on the primary twin system, which occupied <15% of the sample volume (Fig. 7a) when the secondary system nucleated. Twin nucleation in the remaining untwinned volume (85% of the total volume) occurred like in a pristine undeformed crystal and was not influenced by interaction with the primary twins. Therefore, the hardening during this initial stage of deformation (i.e., activation of primary twinning only) is dominated by self hardening with negligible hardening of the latent system. Once additional twin systems are
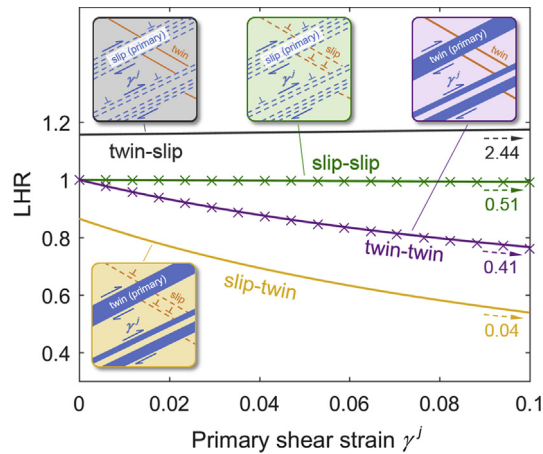
Fig. 8. Dependence of the latent hardening ratio on primary shear strain for the four interactions types according to Equation (10). Solid lines were obtained from the average hardening moduli for 10% of strain (Equation (11)) and crosses from those for 5% of strain. Values on the right border indicate the asymptotic behavior of LHRs for very large γ^j. The insets schematically illustrate the four interaction types when both slip and twinning occur.

activated, the interaction between the primary and secondary twinning triggers latent hardening. Expanding this line of thought we surmise that higher primary twin volume fractions will certainly give rise to interaction with the nucleating secondary system leading to observable latent hardening.

In addition, our analysis revealed significant differences in the self hardening for twinning in the circumstance where both primary and latent twin systems are present and interact vs. where only a single primary system was active. Our calculations in Section 3.5 have shown that when the primary and the latent system are simultaneously active the self hardening modulus, $h_{77}^{twin-twin} = 1.1$ GPa , is almost two times higher than the one associated with isolated primary twinning, $h_{77}^{iso} = 0.65$ GPa. We attribute such differences to sessile residual Burgers vectors produced at the interaction site from the reactions between dislocations associated with primary and latent twin systems, such as those in Table 2. The sessile nature of the residual dislocations impedes not only the growth of the incoming but also of the barrier twin and thus affects the self hardening of both twins. Similar to our observations for twinning, Wu et al. (1991) reported increased self hardening in Cu single crystals in case of double slip compared to single slip. However, for pure slip interactions, the underlying hardening mechanism is different compared to twin-twin interaction due to the absence of interfaces that can act as barriers and incorporate incoming dislocations.

In Table 3, we demonstrate that the magnitude of the residual Burgers vector $|\underline{b}^r|$ engendered from twin-twin incorporation interactions ranges from $0.59a$ to $1.22a$, while that of twin-slip incorporation lies between $0.23a$ and $0.52a$ (Chowdhury et al., 2016; Ezaz et al., 2010; Sangid et al., 2012). The higher $|\underline{b}^r|$ in the case of twin-twin interactions is plausible as it is required to incorporate triplets of incident twinning dislocations to create a step on the barrier twin boundary. When comparing the $|\underline{b}^r|$ values with the corresponding hardening moduli, we note that the $h_{\alpha\beta}^{twin-twin}$ ($\alpha \neq \beta$) values shown in Table 3 are significantly higher than the $h_{\alpha\beta'}^{twin-slip}$ value shown in Equation (B7). Thus, the higher $|\underline{b}^r|$ values for twin-twin interactions are reflected in increased hardening moduli. This result further justifies the key role of residual dislocations played in the strain hardening behavior of the FeMnNiCoCr HEA.

The experimental results shed light into possible avenues for ultrahigh hardening in HEAs. The strengthening levels are comparable to other fcc alloys that are dominated by twinning activity, i.e. the Hadfield steels (Karaman et al., 2001) and Co-Ni alloys (Chowdhury et al., 2016) that have been reported earlier. The exact mechanism for hardening can be alloy specific (such as octahedral to tetrahedral interstitial site exchange during deformation in Hadfield steel). The unique feature of the HEA alloys is that the intrinsic stacking fault energies (SFE) are lower (20–25 mJm^{-2}) (Zaddach et al., 2013) compared to other fcc alloys (i.e. SFE ~100 mJm^{-2} for NiFe (Schramm and Reed, 1976; Zaddach et al., 2013)) on one hand permitting twin nucleation compared to previously studied fcc alloys. Further work is needed in compositional effects (i.e. the role of particles or bcc domains) that could raise the friction stress and hence promote twinning at low strains.

In summary, the use of single crystals and the combination of digital image correlation, electron backscatter diffraction and transmission electron microscopy permit an understanding of the strain hardening phenomena from nano-to micro-meter length scales where activities on multiple twin systems were measured. The current study underscores the key role residual dislocations and the number of activated twin systems played on the strain hardening response of HEAs. The hardening matrices $\{h_{\alpha\beta}\}$ extracted from the experimental results for both $[11\bar{1}]_T$ and $[100]_C$ cases reveal the significance of twin-twin interactions for the overall strengthening of HEAs. It is important to note that the latent hardening moduli $h_{\alpha\beta}^{twin-twin}$ ($\alpha \neq \beta$) arising from twin-twin interactions are more important than the moduli (both self and latent) associated with slip-twin, slip-slip and twin-slip interactions in establishing the overall hardening moduli of a single crystal. The determination of the hardening moduli carried out here will be beneficial for the future plastic modeling of HEAs. As our results have clearly revealed the effect of latent hardening on the overall stress-strain response needs to be considered in any carefully devised hardening description aiming at a physically comprehensive and accurate representation.

5. Conclusions

In summary, the present work supports the following conclusions:

(1) The activation of multiple twin systems results in their interaction and leads to pronounced strain hardening in FeMnNiCoCr HEAs. The higher strain hardening in the $[100]_C$ loading case compared to the $[11\bar{1}]_T$ case is consistent with the activation of a higher number of twin systems and the formation of larger residual Burgers vectors upon their interactions.

(2) The latent hardening moduli for twin-twin interactions are smaller than the self hardening moduli for the respective twin systems when both primary and latent twin systems are present and active.

(3) The self hardening modulus of an isolated twin system is smaller than the twinning self hardening moduli when multiple twin systems are present. We attribute this difference to the residual Burgers vectors, which are brought about by twin-twin interactions and form barriers to the growth of both primary and latent twins.

(4) We demonstrate that the latent hardening moduli for the observed twin-twin interactions are at least one order of magnitude higher than those for slip-slip and slip-twin/twin-slip interactions. This result also verifies the significance of twin-twin interactions to the overall material strengthening and is also consistent with the higher $|\underline{b}^r|$ associated with twin-twin interactions compared to twin-slip interactions.

(5) Plastic deformation modeling of HEA materials needs to account for the latent hardening as a result of twin intersections and the associated effects on flow resistance. The yield criteria must depend on non-glide shear components as well because those stress components affect the primary glide. The HEA alloy single crystal experiments facilitate tracking of the activated systems besides allowing the stress and strain states to be unambiguously defined unlike the polycrystalline case.

Acknowledgements

Appendix A. Considerations of slip-slip and slip-twin/twin-slip interactions

We calculate here the self and latent hardening moduli of slip-slip and slip-twin/twin-slip interactions based on the stress-strain responses included in the previous study by Abuzaid and Sehitoglu (2017). The stress-strain curves of the nominal $[21\bar{2}]_T$ and $[\bar{1}49]_T$ cases are summarized in Fig. A1. The exact crystal orientations determined based on the Euler angles measured from EBSD are [0.7081 0.2991–0.6397] and [-0.0743 0.4462 0.8920], which are denoted as $[21\bar{2}]_T$ and $[\bar{1}49]_T$ thereafter. The designations of the slip and twin systems for an fcc crystal are tabulated in Tables A1 and A2. The self hardening modulus associated with an isolated slip is determined from the $[21\bar{2}]_T$ case where the plastic deformation was accommodated by the single slip system 7′ at the early stage of deformation. The latent hardening moduli for slip-slip interactions are calculated from the $[\bar{1}49]_T$ case where the intersection between slip 3′ and slip 6′ was clearly captured using DIC. Finally, we estimate the $h_{\alpha\beta}$ values for the slip-twin/twin-slip interaction from the $[21\bar{2}]_T$ case where the intersection between slip 7′ and twin 10 was revealed. Fig. A1 illustrates the mechanical responses of the $[21\bar{2}]_T$ and $[\bar{1}49]_T$ loading cases from our previous work on FeMnNiCoCr HEA and the corresponding $h_{\alpha\beta}$ values are marked on the plot as well. The self hardening modulus for an isolated slip system (single slip), $h_{7'7'}^{iso}$, was determined from D to D′ and the latent hardening moduli of the slip-twin and twin-slip interactions, $h_{7'10}^{slip-twin}$ and $h_{107'}^{twin-slip}$, were calculated from E to E' from the stress-strain curve of the $[21\bar{2}]_T$ case. Two examples for twin-slip interaction, where secondary twinning interactions with primary slip, are shown in Fig. A2.

The latent hardening moduli associated with the slip-slip interactions, $h_{3'6'}^{slip-slip}$ and $h_{6'3'}^{slip-slip}$, were determined across the interval F to F' from the stress-strain curve of the $[\bar{1}49]_T$ loading case. We summarize the experiments and intervals from which the $h_{\alpha\beta}$ values were extracted in Table A3. The calculation procedures are elaborated in Appendix B.

Table A1

Designations of all 12 slip systems in an fcc crystal subject to tension along the nominal $[21\bar{2}]_T$ and $[\bar{1}49]_T$ loading orientation. The Schmid factors correspond to the exact loading orientation determined from the Euler angles.

No.	Slip system	Nominal loading direction	
		$[21\bar{2}]_T$	$[\bar{1}49]_T$
		Schmid factor	Schmid factor
1′	$(\bar{1}\bar{1}1)[0\bar{1}\bar{1}]$	0.23	0.28
2′	$(1\bar{1}1)[0\bar{1}\bar{1}]$	0.03	0.20
3′	$(\bar{1}11)[\bar{1}0\bar{1}]$	0.03	**0.46**
4′	$(1\bar{1}1)[\bar{1}01]$	0.13	0.15

5′	$(\bar{1}\bar{1}1)[101]$	0.05	0.17
6′	$(111)[\bar{1}01]$	0.20	**0.48**
7′	$(\bar{1}11)[01\bar{1}]$	**0.41**	0.21
8′	$(\bar{1}11)[\bar{1}\bar{1}0]$	0.38	0.26
9′	$(\bar{1}\bar{1}1)[1\bar{1}0]$	0.27	0.11
10′	$(1\bar{1}1)[\bar{1}\bar{1}0]$	0.09	0.06
11′	$(111)[1\bar{1}0]$	0.06	0.27
12′	$(111)[0\bar{1}1]$	0.14	0.23

Table A2

Designations of all 12 twin systems in an fcc crystal subject to tension along the nominal $[21\bar{2}]_T$ and $[\bar{1}49]_T$ loading orientation. The Schmid factors correspond to the exact loading orientation determined from the Euler angles.

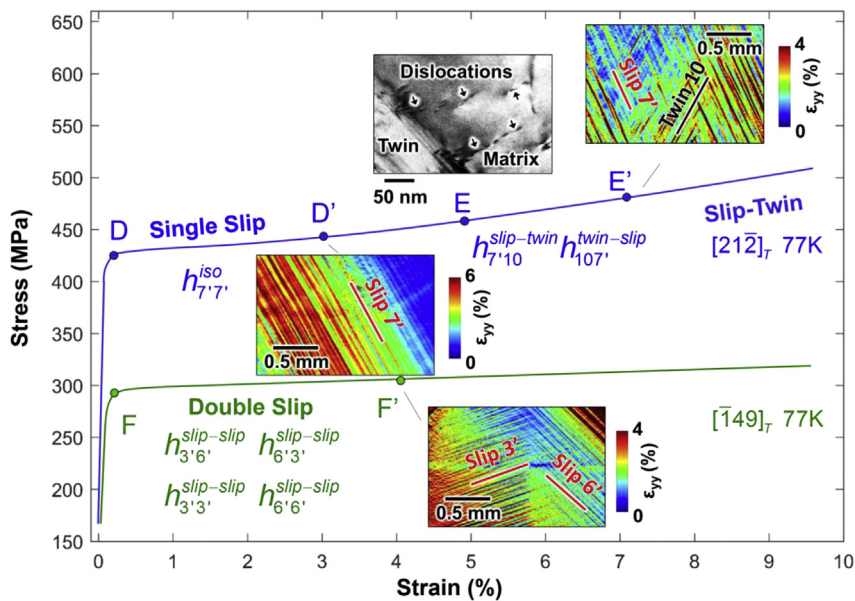| No.	Twin system	Nominal loading direction	
		$[21\bar{2}]_T$	$[\bar{1}49]_T$
		Schmid factor	Schmid factor
1	$(\bar{1}\bar{1}1)[\bar{1}\bar{1}\bar{2}]$	− 0.11	0.44
2	$(1\bar{1}1)[1\bar{1}\bar{2}]$	− 0.09	− 0.02
3	$(\bar{1}11)[\bar{1}1\bar{2}]$	− 0.22	− 0.42
4	$(1\bar{1}1)[121]$	− 0.04	0.04
5	$(\bar{1}\bar{1}1)[\bar{1}21]$	0.29	0.28
6	$(111)[1\bar{2}1]$	− 0.05	− 0.26
7	$(\bar{1}11)[\bar{1}\bar{2}1]$	0.28	0.05
8	$(\bar{1}11)[211]$	− 0.27	0.15
9	$(\bar{1}\bar{1}1)[2\bar{1}1]$	− 0.19	− 0.20
10	$(1\bar{1}1)[\bar{2}\bar{1}1]$	**0.35**	0.39
11	$(111)[\bar{2}11]$	− 0.15	0.02
12	$(111)[11\bar{2}]$	0.20	− 0.42

Fig. A1. The mechanical responses of the FeMnNiCoCr single crystals orientated along $[21\bar{2}]_T$ and $[\bar{1}49]_T$ from previous work by Abuzaid and Sehitoglu (2017). The ex-situ DIC strain contours at different strain levels are included for each case corresponding to slip-slip and slip-twin interaction. The TEM micrograph illustrates the interaction between slip and twinning.
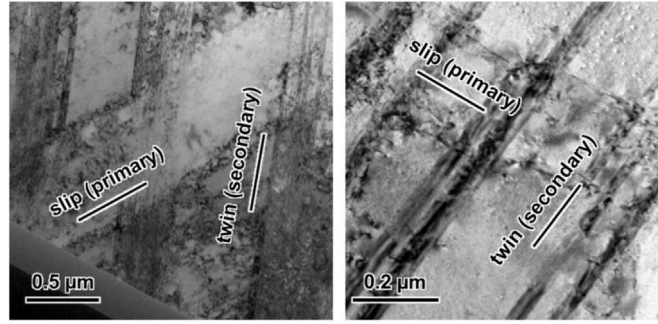
Fig. A2. Two examples for TEM micrographs showing the interaction of secondary twinning with primary slip.

Table A3
A summary of the experiments used to extract the $h_{\alpha\beta}$ values associated with twin-twin, slip-slip and slip-twin interactions.

Twin-Twin	Experiment	Remark
h_{77}^{iso}	[11$\bar{1}$] Tension	A to A′
$h_{77}^{twin-twin}$	[11$\bar{1}$] Tension	B to B′
$h_{1010}^{twin-twin}$	[11$\bar{1}$] Tension	B to B′
$h_{710}^{twin-twin}$ $h_{107}^{twin-twin}$	[11$\bar{1}$] Tension	B to B′
$h_{89}^{twin-twin}$ $h_{98}^{twin-twin}$	[100] Compression	C to C′
$h_{911}^{twin-twin}$ $h_{119}^{twin-twin}$	[100] Compression	C to C′
$h_{811}^{twin-twin}$ $h_{118}^{twin-twin}$	[100] Compression	C to C′
Slip-Slip		
$h_{7'7'}^{iso}$	[21$\bar{2}$] Tension	D to D′
$h_{3'3'}^{slip-slip}$ $h_{6'6'}^{slip-slip}$	[$\bar{1}$49] Tension	F to F′
$h_{3'6'}^{slip-slip}$ $h_{6'3'}^{slip-slip}$	[$\bar{1}$49] Tension	F to F′
Slip-Twin/Twin-Slip		
$h_{7'10}^{slip-twin}$ $h_{107'}^{twin-slip}$	[21$\bar{2}$] Tension	E to E′

Appendix B. Determination of the hardening moduli $h_{\alpha\beta}$ for slip-slip, slip-twin and twin-slip cases

I. Slip-Slip interactions

The self hardening modulus of an isolated slip system in case of single slip, $h_{7'7'}^{iso}$, was determined from D to D' on the stress-strain curve of the $[21\bar{2}]_T$ loading case. Adapting Equation (1) for this particular case, the increment of flow stress is related to the shear strain increment as follows:

$$d\tau_{critical}^{(7')} = h_{7'7'}^{iso} d\gamma_{slip}^{(7')} \tag{B1}$$

After integration, Equation (B1) becomes the following:

$$\int_{m^{(7')}\sigma_D}^{m^{(7')}\sigma_{D'}} d\tau_{critical}^{(7')} = h_{7'7'}^{iso} \int_{\gamma_D^{(7')}}^{\gamma_{D'}^{(7')}} d\gamma_{slip}^{(7')} \tag{B2}$$

where the shear strain at point D′, $\gamma_D^{(7')}$, acting on the slip system 7′ is approximated as $\frac{\varepsilon_{yy}^{(7')}}{m^{(7')}}$ and $\varepsilon_{yy}^{(7')}$ is the local strain determined from the DIC strain contour (see Fig. A1). By solving Equation (B2) with the parameters listed in Table B1, the self hardening coefficient for an isolated slip is calculated as $h_{7'7'}^{iso} = 0.019$ GPa.

Table B1
The stress and strain values used to compute the hardening modulus $h_{7'7'}^{iso}$.

σ_D MPa	$\sigma_{D'}$ MPa	$\varepsilon_{yy}^{(7')}$
412	420	7%

The latent hardening terms, $h_{3'6'}^{slip-slip}$ and $h_{6'3'}^{slip-slip}$, were determined from F to F' on the stress-strain curve of the $[\bar{1}49]_T$ loading case. Similarly, after applying and integrating Equation (1) from F to F', we arrive at the following expressions,

$$\int_{m^{(3')}\sigma_F}^{m^{(3')}\sigma_{F'}} d\tau_{critical}^{(3')} = h_{3'3'}^{slip-slip} \int_{\gamma_F^{(3')}}^{\gamma_{F'}^{(3')}} d\gamma_{slip}^{(3')} + h_{3'6'}^{slip-slip} \int_{\gamma_F^{(6')}}^{\gamma_{F'}^{(6')}} d\gamma_{slip}^{(6')} \tag{B3a}$$

$$\int_{m^{(6')}\sigma_F}^{m^{(6')}\sigma_{F'}} d\tau_{critical}^{(6')} = h_{6'3'}^{slip-slip} \int_{\gamma_F^{(3')}}^{\gamma_{F'}^{(3')}} d\gamma_{slip}^{(3')} + h_{6'6'}^{slip-slip} \int_{\gamma_F^{(6')}}^{\gamma_{F'}^{(6')}} d\gamma_{slip}^{(6')} \tag{B3b}$$

where the shear strains, $\gamma_{F'}^{(3')}$ and $\gamma_{F'}^{(6')}$, acting on the slip systems 3' and 6', respectively, are approximated as $\frac{\varepsilon_{yy}^{(3')}}{m^{(3')}}$ and $\frac{\varepsilon_{yy}^{(6')}}{m^{(6')}}$. Let $h_{3'6'}^{slip-slip} = q h_{6'6'}^{slip-slip}$, $h_{6'3'}^{slip-slip} = q h_{3'3'}^{slip-slip}$ and $h_{6'6'}^{slip-slip} = \Gamma M h_{3'3'}^{slip-slip}$ so that the only unknowns are q and $h_{3'3'}^{slip-slip}$. By solving Equations (B3a) and (B3b) with the parameters listed in Table B2, the unknowns are determined as $q = 0.48$ and $h_{3'3'}^{slip-slip} = 0.023$. The strain hardening coefficients associated with slip-slip interactions are expressed in Equation (B4). Note that the self hardening modulus of the isolated slip system ($h_{7'7'}^{iso} = 0.019$ GPa) is smaller than that of the case where two slip systems are present ($h_{3'3'}^{slip-slip} = 0.023$ GPa). However, both the $h_{7'7'}^{iso}$ and $h_{3'3'}^{slip-slip}$ are significantly smaller than the hardening moduli (self and latent) for the twin-twin case (Table 3).

Table B2
The stress and strain values used to compute the hardening moduli $h_{3'3'}^{slip-slip}$, $h_{3'6'}^{slip-slip}$, $h_{6'3'}^{slip-slip}$ and $h_{6'6'}^{slip-slip}$.

σ_F MPa	$\sigma_{F'}$ MPa	$\varepsilon_{yy}^{(3')}$	$\varepsilon_{yy}^{(6')}$
300	305	3.4%	3.2%

$$\begin{bmatrix} h_{3'3'}^{slip-slip} \\ h_{3'6'}^{slip-slip} \\ h_{6'3'}^{slip-slip} \\ h_{6'6'}^{slip-slip} \end{bmatrix} = \begin{bmatrix} 0.023 \\ 0.012 \\ 0.011 \\ 0.022 \end{bmatrix} \text{GPa} \tag{B4}$$

II. Slip-Twin/Twin-Slip interactions

The latent hardening moduli for slip-twin/twin-slip interactions, $h_{7'10}^{slip-twin}$ and $h_{107'}^{twin-slip}$, were determined from E to E' on the stress-strain curve of the $[21\bar{2}]_T$ loading case. Applying the strain-rate independent crystal plasticity formula in Equation (1) for this particular case, the resolved flow stress increment can be related with the shear strain increment as follows:

$$d\tau_{critical}^{(7')} = h_{7'7'}(1 - f_{twin}^{(10)})d\gamma_{slip}^{(7')} + h_{7'10}^{slip-twin} df_{twin}^{(10)} \gamma_{twin}^{fcc} \tag{B5a}$$

$$d\tau_{critical}^{(10)} = h_{107'}^{twin-slip}(1 - f_{twin}^{(10)})d\gamma_{slip}^{(7')} + h_{1010} df_{twin}^{(10)} \gamma_{twin}^{fcc} \tag{B5b}$$

After integrating Equations (B5a) and (B5b) from E to E', we arrive at the following expressions:

$$\int_{m^{(7')}\sigma_E}^{m^{(7')}\sigma_{E'}} d\tau_{critical}^{(7')} = h_{7'7'}(1 - f_{E'}^{(10)}) \int_{\gamma_E^{(7')}}^{\gamma_{E'}^{(7')}} d\gamma_{slip}^{(7')} + h_{7'10}^{slip-twin} \gamma_{twin}^{fcc} \int_{f_E^{(10)}}^{f_{E'}^{(10)}} df_{twin}^{(10)} \tag{B6a}$$

$$\int_{m^{(10)}\sigma_E}^{m^{(10)}\sigma_{E'}} d\tau_{critical}^{(10)} = h_{107'}^{twin-slip}(1 - f_{E'}^{(10)}) \int_{\gamma_E^{(7')}}^{\gamma_{E'}^{(7')}} d\gamma_{slip}^{(7')} + h_{1010} \gamma_{twin}^{fcc} \int_{f_E^{(10)}}^{f_{E'}^{(10)}} df_{twin}^{(10)} \tag{B6b}$$

where $f_E^{(10)}$ and $f_{E'}^{(10)}$ are the volume fractions of twin 10 at points E and E', respectively. We assumed that the nucleation of the twin system just occurred at point E so that $f_E^{(10)}$ is approximately zero and $f_{E'}^{(10)}$ is approximated from the ex-situ DIC strain contour. It is

also important to note that the ex-situ DIC strain contour associated with the load increment from E to E′ represents the incremental accumulation of plastic strain and not the total strain. The reason for this is that additional surface polishing is required to re-establish a satisfying speckle pattern to enable the continued high-resolution DIC measurement at 77K. Nonetheless, from the local plastic strain, $\varepsilon_{yy}^{(7')}$, associated with the slip system we can still obtain the increase of the shear strain, $\gamma_{E'}^{(7')} - \gamma_E^{(7')} = \frac{\Delta\varepsilon_{yy}^{(7')}}{m^{(7')}}$, for this particular load increment. The shear strain for single slip was also derived from the geometric equation proposed by Bell and Green (Bell and Green Jr, 1967). The result is very close to the one determined from $\frac{\Delta\varepsilon}{m}$ at the considered strain level in this study.

Since the relationship between $h_{7'7'}^{twin-twin}$ and $h_{10\bar{1}0}^{slip-slip}$ $h_{10\bar{1}0}$ is unknown in the case where both slip and twinning are active, we use the values that correspond to the self hardening of an isolated twin and slip in order to gain an insight into the maximum latent moduli, $h_{107'}^{twin-slip}$ and $h_{7'10}^{slip-twin}$:$h_{7'7'}\sim h_{7'7'}^{iso}$, $h_{10\bar{1}0} \sim h_{\bar{1}\bar{1}}^{iso}$. The parameters used to solve Equations (B6a) and (B6b) are tabulated in Table B3 and the resulting hardening moduli are expressed in Equation (B7).

Table B3
The parameters used to compute the hardening moduli $h_{107'}^{twin-slip}$ and $h_{7'10}^{slip-twin}$.

σ_E MPa	$\sigma_{E'}$ MPa	$f_E^{(10)}$	$f_{E'}^{(10)}$	$\varepsilon_{yy}^{(7')}$
450	460	0%	6%	4%

$$\begin{bmatrix} h_{107'}^{twin-slip} \\ h_{7'10}^{slip-twin} \end{bmatrix} = \begin{bmatrix} 0.055 \\ 0.042 \end{bmatrix} \text{GPa} \tag{B7}$$

Appendix C

Considering the earlier literature that evolved around the hardening moduli calculations (Bassani and Wu, 1991; Havner, 1992; Havner and Shalaby, 1977; Wu et al., 1991), it is sufficient to quantify the extent of rotations and demonstrate their possible contributions to the Schmid factors. To clarify this important point, in this appendix section, we aim to present an exemplary analysis which will expound on the $[100]_C$ sample deformation determined from the EBSD measurements on pristine and deformed single crystal.

Table C1
Tabulation of the Euler angles of the pristine and deformed $[100]_C$ sample.

ϕ_1	ϕ	ϕ_2
Pristine $[100]_C$ sample		
0.60°	44.52°	0.55°
Deformed $[100]_C$ sample		
1.53°	46.60°	0.53°

In Table C1, Euler angles {ϕ_1, ϕ, ϕ_2} of the pristine and deformed $[100]_C$ sample via EBSD analysis are tabulated for the pristine and the deformed matrix gage section. These angles are employed to construct the mapping between the cubic frame and the sample frame as follows, where i subscript denotes either the pristine sample or the deformed matrix (Engler and Randle, 2009):

$$G_i = \begin{bmatrix} \cos\phi_2 & \sin\phi_2 & 0 \\ -\sin\phi_2 & \cos\phi_2 & 0 \\ 0 & 0 & 1 \end{bmatrix} \begin{bmatrix} 1 & 0 & 0 \\ 0 & \cos\phi & \sin\phi \\ 0 & -\sin\phi & \cos\phi \end{bmatrix} \begin{bmatrix} \cos\phi_1 & \sin\phi_1 & 0 \\ -\sin\phi_1 & \cos\phi_1 & 0 \\ 0 & 0 & 1 \end{bmatrix} \tag{C1}$$

It is to be noted that $G_{pristine}$ is the coordinate transformation matrix from the pristine sample frame to the cubic frame, and G_{matrix} is the coordinate transformation matrix from the deformed sample frame to the cubic frame. The explicit $G_{pristine}$ and G_{matrix} are expressed as in Equations (C2) and (C3):

$$G_{pristine} = \begin{bmatrix} 0.9998 & 0.0174 & 0.0068 \\ -0.0171 & 0.7128 & 0.7012 \\ 0.0073 & -0.7012 & 0.7129 \end{bmatrix} \tag{C2}$$

$$G_{matrix} = \begin{bmatrix} 0.9994 & 0.0332 & 0.0068 \\ -0.0277 & 0.6866 & 0.7265 \\ 0.0195 & -0.7263 & 0.6871 \end{bmatrix} \tag{C3}$$

The tensor, R, describing the rotation between the pristine and deformed crystals can be expressed as (the superscript index ( )$^{-1}$ corresponds to the matrix inverse operation):

$$R= G_{pristine}^{-1}G_{matrix} \tag{C4}$$

$$R= \begin{bmatrix} 0.9999 & 0.0161 & -0.0006 \\ -0.0161 & 0.9992 & 0.0362 \\ 0.0012 & -0.0362 & 0.9993 \end{bmatrix} \tag{C5}$$

in which the angle of rotation of θ and the rotation axis r correspond to:

$$\theta = \text{acos}\left(\frac{trace(R) - 1}{2}\right) = 2.27^o \tag{C6}$$

$$r= [0.9134\ 0.0227\ 0.4063] \tag{C7}$$

Following the determination of R, the pristine crystal glide direction and plane normal $t_o^{(10)} = [\bar{2}\bar{1}1]/\sqrt{6}$ and $n_o^{(10)} = [1\bar{1}1]/\sqrt{3}$, which correspond to $t^{(10)}$ and $n^{(10)}$ vectors respectively in the deformed configuration, are expressed as (the superscript index ( )$^{-T}$ corresponds to the matrix transpose operation):

$$t^{(10)} = Rt_o^{(10)} = [-0.8232\ -0.3800\ 0.4218] \tag{C8}$$

$$n^{(10)} = R^Tn_o^{(10)} = [0.5872\ -0.5885\ 0.5557] \tag{C9}$$

The modified Schmid factor of the active Twin 10 system in $[100]_C$ sample, $(1\bar{1}1)[\bar{2}\bar{1}1]$, corresponds to 0.4877 and differs from the Schmid factor in the pristine sample by only 0.0163. Similarly, the differentials between the original and modified Schmid factors of the Twin 8, Twin 9 and Twin 11 systems are 0.0155, 0.0168 and 0.0163 respectively in $[100]_C$ sample. Extending the calculations to other samples also yields similar results in the strain regimes in which the corresponding hardening moduli are determined. Although the resulting Schmid factor variations are small, this analysis is required for accurate resolved stress measurements which are significant in the corresponding hardening moduli calculations.

References

Abuzaid, W., Sangid, M.D., Carroll, J.D., Sehitoglu, H., Lambros, J., 2012. Slip Transfer and Plastic Strain Accumulation across Grain Boundaries in Hastelloy X. J. Mech. Phys. Solid. 60, 1201–1220.
Abuzaid, W., Sehitoglu, H., 2017. Critical resolved shear stress for slip and twin nucleation in single crystalline FeNiCoCrMn high entropy alloy. Mater. Char. 129, 288–299.
Alkan, S., Ojha, A., Sehitoglu, H., 2018. Determination of latent hardening response for FeNiCoCrMn for twin-twin interactions. Acta Mater. 147, 149–164.
Asaro, R.J., 1983. Micromechanics of crystals and polycrystals. In: Hutchinson, J.W., Wu, T.Y. (Eds.), Advances in Applied Mechanics. Elsevier, pp. 1–115.
Bassani, J.L., Wu, T.-Y., 1991. Latent hardening in single crystals. II. Analytical characterization and predictions. Proc. Roy. Soc. Lond. A 21–41 The Royal Society.
Bell, J.F., Green Jr., R.E., 1967. An experimental study of the double slip deformation hypothesis for face-centred cubic single crystals. Phil. Mag. 15, 469–476.
Bertin, N., Tomé, C.N., Beyerlein, I.J., Barnett, M.R., Capolungo, L., 2014. On the strength of dislocation interactions and their effect on latent hardening in pure Magnesium. Int. J. Plast. 62, 72–92.
Brahme, A.P., Inal, K., Mishra, R.K., Saimoto, S., 2011. A new strain hardening model for rate-dependent crystal plasticity. Comput. Mater. Sci. 50, 2898–2908.
Cantor, B., Chang, I., Knight, P., Vincent, A., 2004. Microstructural development in equiatomic multicomponent alloys. Mater. Sci. Eng. A 375, 213–218.
Carroll, J., Abuzaid, W., Lambros, J., Sehitoglu, H., 2010. An experimental methodology to relate local strain to microstructural texture. Rev. Sci. Instrum. 81.
Cherkaoui, M., 2003. Constitutive equations for twinning and slip in low-stacking-fault-energy metals: a crystal plasticity-type model for moderate strains. Phil. Mag. 83, 3945–3958.
Chowdhury, P., Sehitoglu, H., Maier, H., Rateick, R., 2016. Strength prediction in NiCo alloys–the role of composition and nanotwins. Int. J. Plast. 79, 237–258.
Efstathiou, C., Sehitoglu, H., 2010. Strain hardening and heterogeneous deformation during twinning in Hadfield steel. Acta Mater. 58, 1479.
Engler, O., Randle, V., 2009. Introduction to Texture Analysis: Macrotexture, Microtexture, and Orientation Mapping. CRC press.
Ezaz, T., Sangid, M.D., Sehitoglu, H., 2010. Energy barriers associated with slip-twin interactions. Phil. Mag. 91, 1464–1488.
Franciosi, P., 1983. Glide mechanisms in b.c.c. crystals: an investigation of the case of α-iron through multislip and latent hardening tests. Acta Metall. 31, 1331–1342.
Franciosi, P., 1985. The concepts of latent hardening and strain hardening in metallic single crystals. Acta Metall. 33, 1601–1612.
Franciosi, P., Berveiller, M., Zaoui, A., 1980. Latent hardening in copper and aluminium single crystals. Acta Metall. 28, 273–283.
Friedel, J., 1955. CXXX. On the linear work hardening rate of face-centred cubic single crystals. Lond., Edinb. Dublin Phil. Mag. J. Sci. 46, 1169–1186.
Gali, A., George, E.P., 2013. Tensile properties of high- and medium-entropy alloys. Intermetallics 39, 74–78.
Gludovatz, B., Hohenwarter, A., Catoor, D., Chang, E.H., George, E.P., Ritchie, R.O., 2014. A fracture-resistant high-entropy alloy for cryogenic applications. Science 345, 1153–1158.
Havner, K.S., 1992. Finite Plastic Deformation of Crystalline Solids. Cambridge University Press.
Havner, K.S., Shalaby, A.H., 1977. A simple mathematical theory of finite distortional latent hardening in single crystals. Proc. Roy. Soc. Lond. A 47–70 The Royal Society.
Hazeli, K., Cuadra, J., Vanniamparambil, P., Kontsos, A., 2013. In situ identification of twin-related bands near yielding in a magnesium alloy. Scripta Mater. 68, 83–86.
Hill, R., 1966. Generalized constitutive relations for incremental deformation of metal crystals by multislip. J. Mech. Phys. Solid. 14, 95–102.
Hirth, J., 1961. On dislocation interactions in the fcc lattice. J. Appl. Phys. 32, 700–706.
Hutchinson, J., 1970. Elastic-plastic behaviour of polycrystalline metals and composites. Proc. Roy. Soc. Lond. A Math. Phys. Eng. Sci. 247–272 The Royal Society.
Iadicola, M.A., Hu, L., Rollett, A.D., Foecke, T., 2012. Crystal plasticity analysis of constitutive behavior of 5754 aluminum sheet deformed along bi-linear strain paths. Int. J. Solid Struct. 49, 3507–3516.
Jackson, P., Basinski, Z., 1967. Latent hardening and the flow stress in copper single crystals. Can. J. Phys. 45, 707–735.
Jin, Z.H., Gumbsch, P., Albe, K., Ma, E., Lu, K., Gleiter, H., Hahn, H., 2008. Interactions between non-screw lattice dislocations and coherent twin boundaries in face-centered cubic metals. Acta Mater. 56, 1126.
Karaman, I., Sehitoglu, H., Chumlyakov, Y.I., Maier, H.J., Kireeva, I., 2001. The effect of twinning and slip on the Bauschinger effect of Hadfield steel single crystals.

Metall. Mater. Trans. A 32, 695–706.

Kireeva, I.V., Chumlyakov, Y.I., Pobedennaya, Z.V., Platonova, Y.N., Kuksgauzen, I.V., Kuksgauzen, D.A., Poklonov, V.V., Karaman, I., Sehitoglu, H., 2016. Slip and twinning in the [-149]-Oriented single crystals of a high-entropy alloy. Russ. Phys. J. 59, 1242–1250.

Kocks, U., 1970. The relation between polycrystal deformation and single-crystal deformation. Metall. Mater. Trans. B 1, 1121–1143.

Kocks, U.F., Brown, T.J., 1966. Latent hardening in aluminum. Acta Metall. 14, 87–98.

Laplanche, G., Kostka, A., Horst, O., Eggeler, G., George, E., 2016. Microstructure evolution and critical stress for twinning in the CrMnFeCoNi high-entropy alloy. Acta Mater. 118, 152–163.

Mahajan, S., Chin, G., 1973. Twin-slip, twin-twin and slip-twin interactions in Co-8 wt.% Fe alloy single crystals. Acta Metall. 21, 173–179.

Mahajan, S., Chin, G., 1974. The interaction of twins with existing substructure and twins in cobalt-iron alloys. Acta Metall. 22, 1113–1119.

Mandel, J., 1965. Generalisation de la theorie de plasticite de W. T. Koiter. Int. J. Solid Struct. 1, 273–295.

Mott, N.F., 1952. CXVII. A theory of work-hardening of metal crystals. Lond., Edinb. Dublin Phil. Mag. J. Sci. 43, 1151–1178.

Nakada, Y., Keh, A.S., 1966. Latent hardening in iron single crystals. Acta Metall. 14, 961–973.

Otto, F., Dlouhý, A., Somsen, C., Bei, H., Eggeler, G., George, E.P., 2013a. The influences of temperature and microstructure on the tensile properties of a CoCrFeMnNi high-entropy alloy. Acta Mater. 61, 5743–5755.

Otto, F., Yang, Y., Bei, H., George, E.P., 2013b. Relative effects of enthalpy and entropy on the phase stability of equiatomic high-entropy alloys. Acta Mater. 61, 2628–2638.

Patriarca, L., Abuzaid, W., Sehitoglu, H., Maier, H.J., Chumlyakov, Y., 2013. Twin nucleation and migration in FeCr single crystals. Mater. Char. 75, 165–175.

Peirce, D., Asaro, R.J., Needleman, A., 1982. An analysis of nonuniform and localized deformation in ductile single crystals. Acta Metall. 30, 1087–1119.

Pettersen, E.F., Goddard, T.D., Huang, C.C., Couch, G.S., Greenblatt, D.M., Meng, E.C., Ferrin, T.E., 2004. UCSF Chimera—a visualization system for exploratory research and analysis. J. Comput. Chem. 25, 1605–1612.

Pham, M.S., Creuziger, A., Iadicola, M., Rollett, A.D., 2017. Roles of texture and latent hardening on plastic anisotropy of face-centered-cubic materials during multi-axial loading. J. Mech. Phys. Solid. 99, 50–69.

Remy, L., 1977. Twin-twin interaction in FCC crystals. Scripta Metall. 11, 169–172.

Remy, L., 1981. The interaction between slip and twinning systems and the influence of twinning on the mechanical behavior of fcc metals and alloys. Metall. Mater. Trans. A 12, 387–408.

Salem, A., Kalidindi, S., Semiatin, S., 2005. Strain hardening due to deformation twinning in α-titanium: constitutive relations and crystal-plasticity modeling. Acta Mater. 53, 3495–3502.

Sangid, M.D., Ezaz, T., Sehitoglu, H., 2012. Energetics of residual dislocations associated with slip–twin and slip–GBs interactions. Mater. Sci. Eng. A 542, 21–30.

Schmid, E., Boas, W.M., 1935. Kristallplastizität: mit besonderer Berücksichtung der Metalle. Verlag von Julius Springer.

Schramm, R.E., Reed, R.P., 1976. Stacking fault energies of fcc fe-Ni alloys by x-ray diffraction line profile analysis. Metallur. Trans. A 7, 359–363.

Seeger, A., Diehl, J., Mader, S., Rebstock, H., 1957. Work-hardening and work-softening of face-centred cubic metal crystals. Phil. Mag. 2, 323–350.

Tadano, Y., Yoshihara, Y., Hagihara, S., 2016. A crystal plasticity modeling considering volume fraction of deformation twinning. Int. J. Plast. 84, 88–101.

Taylor, G.I., F, R.S., Elam, C.F., 1923. Bakerian Lecture: the distortion of an aluminium crystal during a tensile test. Proc. Roy. Soc. Lond. A 643–667 The Royal Society.

Wessels, E.J.H., Jackson, P.J., 1969. Latent hardening in copper-aluminium alloys. Acta Metall. 17, 241–248.

Wessels, E.J.H., Nabarro, F.R.N., 1971. The hardening of latent glide systems in single crystals of copper-aluminium alloys. Acta Metall. 19, 903–914.

Wu, T.-Y., Bassani, J.L., Laird, C., 1991. Latent hardening in single crystals I. Theory and experiments. Proc. Roy. Soc. Lond. A Math. Phys. Eng. Sci. 1–19 The Royal Society.

Wu, Z., Parish, C., Bei, H., 2015. Nano-twin mediated plasticity in carbon-containing FeNiCoCrMn high entropy alloys. J. Alloy. Comp. 647, 815–822.

Zaddach, A., Niu, C., Koch, C., Irving, D., 2013. Mechanical properties and stacking fault energies of NiFeCrCoMn high-entropy alloy. JOM (J. Occup. Med.) 65, 1780–1789.

Zhang, Z., Mao, M., Wang, J., Gludovatz, B., Zhang, Z., Mao, S.X., George, E.P., Yu, Q., Ritchie, R.O., 2015. Nanoscale origins of the damage tolerance of the high-entropy alloy CrMnFeCoNi. Nat. Commun. 6, 10143.